

Abstract

The meteorological characteristics of cloudy atmospheric columns can be very different from their clear counterparts. Thus, when a forecast ensemble is uncertain about the presence/absence of clouds at a specific atmospheric column (*i.e.*, some members are clear while others are cloudy), that column's ensemble statistics will contain a mixture of clear and cloudy statistics. Such mixtures are inconsistent with the ensemble data assimilation algorithms currently used in numerical weather prediction. Hence, ensemble data assimilation algorithms that can handle such mixtures can potentially outperform currently used algorithms.

In this study, we demonstrate the potential benefits of addressing such mixtures through a bi-Gaussian extension of the ensemble Kalman filter (BGENKF). The BGENKF is compared against the commonly used ensemble Kalman filter (EnKF) using perfect model observing system simulated experiments (OSSEs) with a realistic weather model (the Weather Research and Forecast model). Synthetic all-sky infrared radiance observations are assimilated in this study. In these OSSEs, the BGENKF outperforms the EnKF in terms of the horizontal wind components, temperature, specific humidity, and simulated upper tropospheric water vapor channel infrared brightness temperatures.

This study is one of the first to demonstrate the potential of a Gaussian mixture model EnKF with a realistic weather model. Our results thus motivate future research towards improving numerical Earth system predictions though explicitly handling mixture statistics.

Plain Language Summary

The accuracy of a computer weather forecast often depends on the accuracy of the information inputted into the computer forecast system. The accuracy of the input in turn depends on the accuracy of the input-constructing algorithm. Such algorithms often use probabilistic forecasts from an earlier point in time and current atmospheric measurements to construct the inputs.

A common assumption in input-constructing algorithms is that the probabilistic forecasts follow multivariate normal distributions (henceforth called the normality assumption). However, in the frequent situation where the probabilistic forecasts are uncertain about the presence/absence of clouds, the normality assumption is violated. This is because clear atmospheric columns and cloudy atmospheric columns have distinctly different thermodynamic and dynamic characteristics. Such probabilistic forecasts thus have mixed statistics (henceforth termed mixed probabilistic forecasts). Addressing these mixed statistics can potentially improve forecasts.

In this study, we propose a new input-constructing algorithm that can explicitly handle mixed probabilistic forecasts. Compared to an existing popular algorithm, our algorithm is nearly as fast and can produce more accurate forecast inputs. Our work thus suggests that weather forecasts can be improved by upgrading input-constructing algorithms to treat a common situation where the normality assumption is violated.

1 Introduction

Earth system analysis and forecasting systems rely on ensemble data assimilation (ensemble DA, or EDA) methods to convert observations into corrections for Earth system model variables (Keppenne et al., 2005; Reichle et al., 2009; Edwards et al., 2015; Stammer et al., 2016; Park & Xu, 2016; ECMWF, 2016; Helmert et al., 2018; Hersbach et al., 2020). Current operational EDA methods typically assume that every member in an input forecast ensemble is drawn from a distribution only containing a single Gaussian kernel [*i.e.*, a Gaussian distribution; henceforth termed the unmixed ensemble assumption; *e.g.*, Geer et al. (2018) and Dowell et al. (2022)]. The effectiveness of such methods can thus be limited by the validity of this assumption.

The unmixed ensemble assumption is violated for ensembles that are uncertain about the presence or absence of clouds at any model grid point. This is because clear atmospheric columns and cloudy atmospheric columns often have different dynamic, thermodynamic, and radiative properties [*e.g.*, Emanuel (1994), Markowski and Richardson (2010)]. Cloudy statistics are thus often different from clear statistics [*e.g.*, Grimes and Pardo-Igúzquiza (2010); Geer and Bauer (2011)]. If some ensemble members are cloudy at a location, and other members are clear at this location, the ensemble can exhibit mixed statistics (Harnisch et al., 2016; Minamide & Zhang, 2017; Honda et al., 2018; Chan, Anderson, & Chen, 2020). More evidence of mixed statistics can be found in the supporting information. The effectiveness of current operational EDA methods is likely limited in such situations.

This limitation can be mitigated by extending current operational EDA methods to handle mixed statistics. One possibility is to extend the commonly used ensemble Kalman filter, or the EnKF (Evensen, 1994; P. L. Houtekamer & Mitchell, 1998; Burgers et al., 1998; Tippett et al., 2003; Anderson, 2003; Whitaker & Hamill, 2002; Keppenne et al., 2005; Hunt et al., 2007; Reichle et al., 2009; Stammer et al., 2016; Edwards et al., 2015; Park & Xu, 2016; Helmert et al., 2018), to handle members drawn from forecast distributions with two Gaussian kernels. Specifically, we assume that forecast members that are clear at an observation site (henceforth, clear members) are drawn from one Gaussian kernel, and forecast members that are cloudy at this site (henceforth, cloudy members) are drawn from a different Gaussian kernel. This bi-Gaussian extension of the EnKF (henceforth, the BGenKF) allows the clear ensemble statistics to be handled separately from the cloudy ensemble statistics (Chan, Anderson, & Chen, 2020), thus addressing the issue of mixed statistics.

We recently proposed a computationally efficient BGenKF to handle mixtures of clear and cloudy members [Chan, Anderson, and Chen (2020); henceforth, the CAC20 BGenKF]. Unlike similar methods proposed in the past (Dovera & Della Rossa, 2011; Reich, 2012; Sondergaard & Lermusiaux, 2013a, 2013b), the CAC20 BGenKF does not use an expectation maximization (EM) algorithm to estimate the mean and covariances of the two Gaussian kernels. Instead, the CAC20 BGenKF assigns the the sample mean and covariances of the cloudy members to one Gaussian kernel, and those of the clear members to the other Gaussian kernel. This assignment circumvents the computational cost and issues associated with using the EM algorithm in high dimensional spaces [see Chan, Anderson, and Chen (2020) for more information]. Furthermore, the CAC20 BGenKF converts clear members into cloudy members, or *vice versa*, without involving the costly square-root computations or Cholesky decompositions of high-dimensional forecast covariance matrices.

The purpose of this study is to demonstrate that a variant of the CAC20 BGenKF can outperform the EnKF using a realistic high-order weather model (the Weather Research and Forecast model; WRF). To do so, this new BGenKF is implemented into the state-of-the-art Pennsylvania State University EnKF system [henceforth, the PSU-EnKF system; Meng and Zhang (2007, 2008), Chan, Zhang, et al. (2020)]. This demonstration is done using perfect model observing system simulation experiments (OSSEs) of a case of tropical convection over the equatorial Indian Ocean. This case occurred during the onset of the active phase of

111 the October 2011 Madden-Julian Oscillation event [MJO; Madden and Julian (1971, 1972),
112 and S. Wang et al. (2015)].

113 The structure of this paper is as follows. In section 2, we will give an overview of the
114 BGenKF algorithm, discuss how clear and cloudy members are identified, and modifications
115 made to the CAC20 BGenKF algorithm. A detailed description of the current BGenKF,
116 along with suggestions on handling more than two Gaussian kernels, can be found in the sup-
117 porting information. Following that, we will discuss the setup of our OSSEs in section 3 and
118 the results in section 4. We will then conclude in section 5.

119 **2 On the BGenKF algorithm**

120 **2.1 On the identification of clear and cloudy members**

121 The BGenKF requires identifying clear and cloudy members at each iteration of the
122 serial data assimilation loop. A simple identification method is to check if the members’
123 column-integrated liquid and/or frozen water mass contents exceed a threshold.

124 The choice of which phase of water to include in the column integration depends on
125 the specifics of the forecast model. As will be discussed in section 3.3, this study used a
126 WRF model setup with a 9-km horizontal grid spacing and without convective parameter-
127 ization. This WRF model setup cannot realistically resolve trade cumuli since the typical
128 width of trade cumuli is ~ 1 -km. As such, we consider columns with trade cumuli and en-
129 tirely cloud-free columns as clear member columns, and the remaining members as cloudy
130 member columns. Since trade cumuli do not typically grow above the melting layer (Johnson
131 et al., 1999), clear members do not possess frozen water. It thus seems appropriate to use
132 column-integrated ice mass content (ξ) to distinguish between clear and cloudy member
133 columns. To be precise, we compute ξ at a given model column via

$$\xi \equiv \int_0^{z_{top}} \rho(q_i + q_s + q_g) dz \quad (1)$$

134 where z_{top} is the model top altitude and ρ represents air density. Furthermore, q_i , q_s and q_g
135 are the mass mixing ratios of ice, snow and graupel, respectively.

136 In this study, we will consider model columns with $\xi \geq 1 \text{ g/m}^2$ as cloudy, and model
137 columns with $\xi < 1 \text{ g/m}^2$ as clear. The cloudy and clear infrared window channel simulated
138 brightness temperature statistics (Window-BT; central wavelength of $10.5 \mu\text{m}$) do not vary
139 noticeably for model column ξ thresholds between 0.8 - 1.2 g/m^2 . Future studies can refine
140 the threshold value or seek better ways to separate clear and cloudy column members.

141 **2.2 Overview of the BGenKF algorithm**

142 This study’s BGenKF (and the CAC20 BGenKF) assimilates observations with Gaus-
143 sian observation likelihoods under the assumption that clear members are drawn from one
144 Gaussian kernel and cloudy members are drawn from another Gaussian kernel. Suppose we
145 seek to constrain the following extended state vector ψ

$$\psi \equiv \begin{bmatrix} \mathbf{x} \\ \mathbf{h}(\mathbf{x}) \\ \xi(\mathbf{x}) \end{bmatrix} \quad (2)$$

146 where \mathbf{x} represents the model state, $\mathbf{h}(\mathbf{x})$ represents applying the observation operator \mathbf{h} on
147 \mathbf{x} , and $\xi(\mathbf{x})$ represents computing ξ at all observation sites [Eq. (1)]. Note that observation
148 sites here refers to the latitude and longitude of the observation (*i.e.*, the vertical position is
149 not considered for now). Supposing there are N_x elements in \mathbf{x} and N_y observations, then ψ
150 has $N_x + 2N_y$ elements.

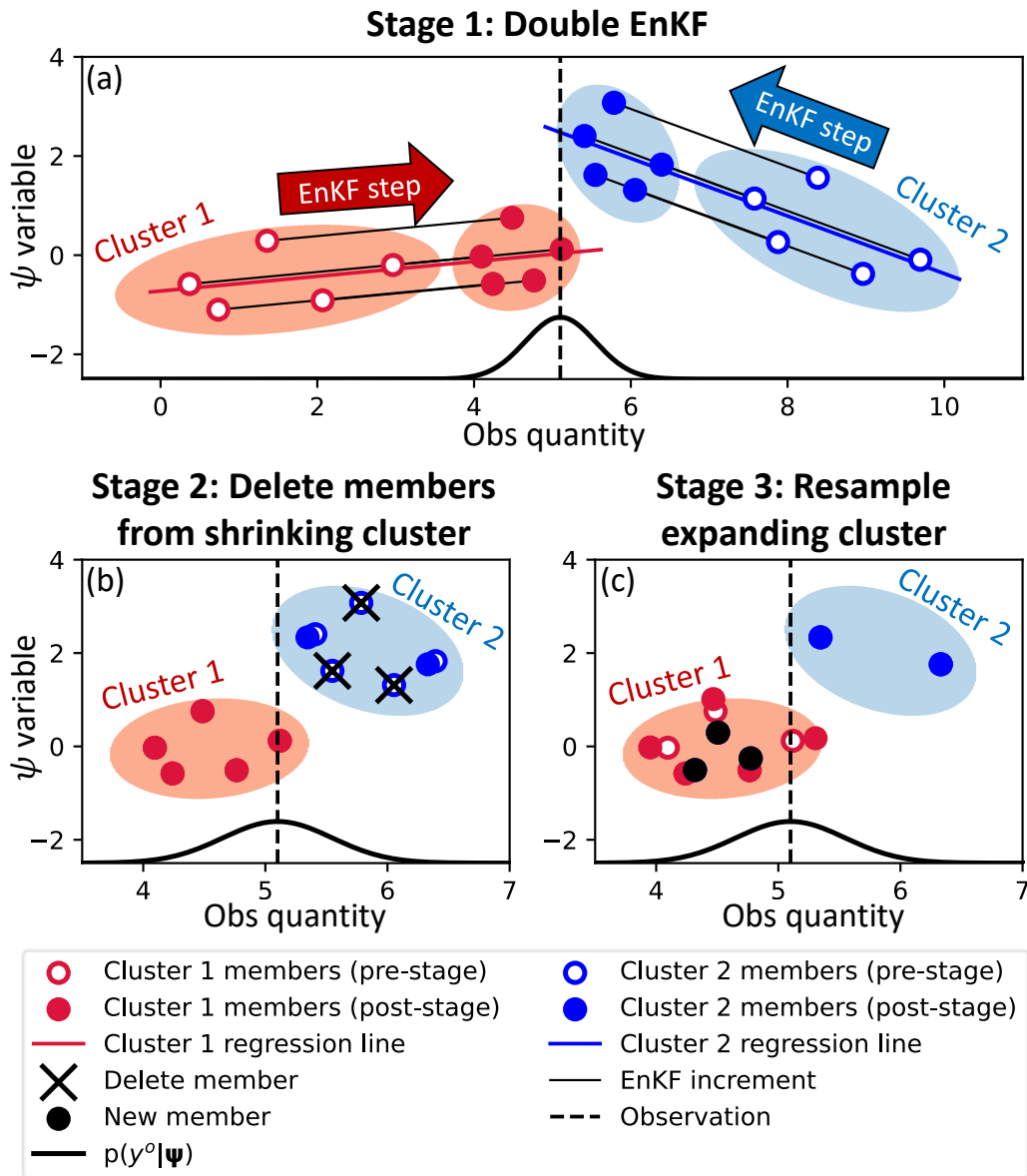


Figure 1. A bivariate demonstration of the three-stage process of the BGenKF algorithm. The light red ovals highlight cluster 1 members and the light blue ovals highlight cluster 2 members. Prior to running the BGenKF update, the prior members have already been separated into two clusters. The BGenKF’s first stage is to employ the EnKF update equations on the two clusters separately (panel a). In the second stage (panel b), the BGenKF identifies the shrinking cluster (the blue cluster 2 in this case), deletes an appropriate number of members from this cluster, and adjusts the remaining members to prevent the deletion from changing this cluster’s mean. The BGenKF’s final stage (panel c) is to recreate the deleted members by resampling from the expanding cluster (cluster 1).

151 The BGenKF assumes that the prior probability density function [pdf; $p(\boldsymbol{\psi})$] can be
 152 represented by the bi-Gaussian pdf

$$p(\boldsymbol{\psi}) = w_{\text{clr}}^f \mathcal{G}\left(\boldsymbol{\psi}; \overline{\boldsymbol{\psi}}_{\text{clr}}^f, \mathbf{P}_{\text{clr}}^f\right) + w_{\text{cld}}^f \mathcal{G}\left(\boldsymbol{\psi}; \overline{\boldsymbol{\psi}}_{\text{cld}}^f, \mathbf{P}_{\text{cld}}^f\right). \quad (3)$$

The subscript ‘‘clr’’ denotes clear cluster quantities, and the subscript ‘‘cld’’ denotes cloudy cluster quantities. $\mathcal{G}\left(\boldsymbol{\psi}; \overline{\boldsymbol{\psi}}_{\text{clr}}^f, \mathbf{P}_{\text{clr}}^f\right)$ denotes the clear cluster’s Gaussian kernel with mean state $\overline{\boldsymbol{\psi}}_{\text{clr}}^f$ and covariance matrix $\mathbf{P}_{\text{clr}}^f$. Similarly, $\mathcal{G}\left(\boldsymbol{\psi}; \overline{\boldsymbol{\psi}}_{\text{cld}}^f, \mathbf{P}_{\text{cld}}^f\right)$ denotes the cloudy cluster’s Gaussian kernel with mean state $\overline{\boldsymbol{\psi}}_{\text{cld}}^f$ and covariance matrix $\mathbf{P}_{\text{cld}}^f$. The scalar quantities w_{clr}^f and w_{cld}^f are the respective weights of the clear and cloudy Gaussian kernels. Note that

$$w_{\text{clr}}^f + w_{\text{cld}}^f = 1, \quad w_{\text{clr}}^f \geq 0, \quad \text{and}, \quad w_{\text{cld}}^f \geq 0.$$

153 The various parameters in Eq. (3) can be estimated by the procedure described in CAC20 or
 154 in the supporting information.

155 Upon assimilating an observation y^o with Gaussian observation error, the BGenKF
 156 produces an ensemble that is consistent with the analysis pdf

$$p(\boldsymbol{\psi}|y^o) = w_{\text{clr}}^a \mathcal{G}\left(\boldsymbol{\psi}; \overline{\boldsymbol{\psi}}_{\text{clr}}^a, \mathbf{P}_{\text{clr}}^a\right) + w_{\text{cld}}^a \mathcal{G}\left(\boldsymbol{\psi}; \overline{\boldsymbol{\psi}}_{\text{cld}}^a, \mathbf{P}_{\text{cld}}^a\right). \quad (4)$$

157 Here, w_{clr}^a and w_{cld}^a are the respective analysis weights of clear and cloudy Gaussian kernels,
 158 $\overline{\boldsymbol{\psi}}_{\text{clr}}^a$ and $\overline{\boldsymbol{\psi}}_{\text{cld}}^a$ are the respective analysis means of the clear and cloudy Gaussian kernels, and
 159 $\mathbf{P}_{\text{clr}}^a$ and $\mathbf{P}_{\text{cld}}^a$ are the respective analysis covariances of the clear and cloudy Gaussian kernels.
 160 See CAC20 [or the supporting information] for the equations relating the analysis pdf’s
 161 parameters to the forecast pdf’s parameters.

162 The BGenKF converts a forecast ensemble into an analysis ensemble through a three-
 163 stage process [illustrated in Figure 1]. First, two EnKF procedures are executed [Figure
 164 1(a)]: once for clear members using clear forecast statistics $\left(\overline{\boldsymbol{\psi}}_{\text{clr}}^f, \mathbf{P}_{\text{clr}}^f\right)$, and a second time
 165 for cloudy members using cloudy forecast statistics $\left(\overline{\boldsymbol{\psi}}_{\text{cld}}^f, \mathbf{P}_{\text{cld}}^f\right)$. Afterwards, to reflect the
 166 update to the bi-Gaussian pdf weights, clear members will be replaced with cloudy members,
 167 or *vice versa*. For example, if the BGenKF increased the weight on the clear Gaussian distri-
 168 bution (*i.e.*, $w_{\text{clr}}^a > w_{\text{clr}}^f$ and $w_{\text{cld}}^a < w_{\text{cld}}^f$), some cloudy members will be replaced with clear
 169 members. This is achieved by deleting some cloudy members [Figure 1(b)] and replacing
 170 the deleted members with resampled clear members [Figure 1(c)]. Once these three stages
 171 are completed, the ensemble obeys Eq. (4). See the supporting information for a detailed
 172 description of these three stages.

173 2.3 Revised extended state formulation for better scalable parallelism

174 The most important modification to the original CAC20 BGenKF lies in the defini-
 175 tion of $\boldsymbol{\psi}$. The CAC20 BGenKF’s $\boldsymbol{\psi}$ only contains \mathbf{x} and a single observation. As such, the
 176 CAC20 BGenKF algorithm is a sequential algorithm that scales inefficiently with paral-
 177 lelization on high latency clusters (Anderson & Collins, 2007). For more efficient scaling
 178 with parallelization, this study’s $\boldsymbol{\psi}$ contains all of the information necessary to assimilate all
 179 observations [*i.e.*, Eq. (2); Anderson and Collins (2007)].

180 Since the definition of $\boldsymbol{\psi}$ has been modified, we will redefine our forecast ensemble.
 181 Supposing an ensemble size of N_E , the forecast $\boldsymbol{\psi}$ ensemble is constructed by evaluating

$$\boldsymbol{\psi}_n^f \equiv \begin{bmatrix} x_n^f \\ \mathbf{h}(x_n^f) \\ \boldsymbol{\xi}(x_n^f) \end{bmatrix} \quad \forall n = 1, 2, \dots, N_E \quad (5)$$

where ψ_n^f is the ψ of the n -th forecast member, and x_n^f is the x of the same forecast member.

The revised formulation enhances the scalability of the BGenKF by avoiding evaluations of $h(x)$ and $\xi(x)$ at each iteration of the serial assimilation loop. This is because such evaluations may require costly inter-process communications. The removal of such evaluations is achieved through two modifications to the CAC20 BGenKF. First, the assimilation of an observation uses the BGenKF update equations (see CAC20 or the supporting information) to update all model state elements, all simulated observation state elements and all ξ elements in the forecast ensemble. The CAC20 BGenKF, in contrast, updates all model state elements and only a single simulated observation state element. This difference in updates leads to a second modification: to assimilate the m -th observation, instead of evaluating $h(x)$ and $\xi(x)$, this study's BGenKF only needs to read the corresponding simulated observation and the ξ values from ψ .

2.4 Revised expanding cluster resampling procedure

The other major change to the CAC20 BGenKF lies in the resampling matrix T . T is used to resample the Gaussian kernel that better agrees with the assimilated observation, thus representing the increase in the weight of this kernel. The CAC20 BGenKF uses a stochastic procedure to construct T [see Eq. (18) and Appendix B of CAC20]. Unfortunately, because random number generators are involved, the analysis ensemble generated on one computing cluster may not be easily replicated on another computing cluster.

To ensure the replicability of the BGenKF's analysis ensembles, we replaced the stochastic component of the CAC20 BGenKF's T [W in the Appendix B of Chan, Anderson, and Chen (2020)] with a deterministic one. Supposing that we want to add N_{new} cloudy members to the ensemble to represent an increased weight of the cloudy Gaussian distribution, the new deterministic W is defined as

$$W \equiv \left[\begin{array}{cc} I_{N_{\text{new}}^*} & \mathbf{0}_{N_{\text{new}}^* \times (N_{\text{new}} - N_{\text{new}}^*)} \end{array} \right] - \frac{1}{N_{\text{new}}} \mathbf{1}_{N_{\text{new}}^* \times N_{\text{new}}} \quad (6)$$

where

$$N_{\text{new}}^* \equiv \begin{cases} N_{\text{new}} - 1 & \forall N_{\text{new}} \leq N_{\text{pre}} \\ N_{\text{pre}} & \text{otherwise} \end{cases},$$

and N_{pre} is the number of cloudy members at the start of the resampling procedure. Furthermore, $I_{N_{\text{new}}^*}$ is an $N_{\text{new}}^* \times N_{\text{new}}^*$ identity matrix, $\mathbf{0}_{N_{\text{new}}^* \times (N_{\text{new}} - N_{\text{new}}^*)}$ is an $N_{\text{new}}^* \times (N_{\text{new}} - N_{\text{new}}^*)$ matrix of zeros, and $\mathbf{1}_{N_{\text{new}}^* \times N_{\text{new}}}$ is an $N_{\text{new}}^* \times N_{\text{new}}$ matrix of ones. Note that Eq. (6) is also applied in the situation where N_{new} clear members are being added to the ensemble. A detailed description of the revised resampling procedure is provided in the supporting information.

Note that an interesting property of Eq. (6) is that the resulting T is a mostly diagonal matrix. Specifically, nearly all of the off-diagonal elements in T are either zero or much smaller than the diagonal elements (not shown). As a result, the resampled members are essentially copies of the pre-resampling members, plus some small perturbation. The CAC20 stochastic W formulation does not have this property. Future work can investigate how the BGenKF's behavior changes with different W formulations.

2.5 Heuristic measures

2.5.1 Localization

The BGenKF is likely more susceptible to sampling noise than the EnKF because the sample size used to estimate each cluster's mean state and Kalman gain are smaller than the sample size used to estimate the mean state and covariance matrix of the entire ensemble. As such, we employ two heuristic measures that are similar to those of CAC20. First, we

223 spatially localize the BGenKF analysis increment using the Gaspari-Cohn fifth order poly-
 224 nomial [GC99; Gaspari and Cohn (1999)]. If ρ represents a vector of GC99 localization factors,
 225 we construct the localized updated extended state vector for member n via

$$\psi_n^a \leftarrow \rho \circ (\psi_n^a - \psi_n^f) + \psi_n^f \quad (7)$$

226 where \circ represents element-wise multiplication. In the cases where either $w_{\text{clr}}^f = 1$ or $w_{\text{cld}}^f =$
 227 1 (*i.e.*, the bi-Gaussian prior p.d.f. turns Gaussian), this localization method is identical to
 228 Kalman gain localization [*e.g.*, Anderson et al. (2009), Meng and Zhang (2008), Whitaker et
 229 al. (2008), P. L. Houtekamer and Zhang (2016)].

230 Note that this localization method [Eq. (7)] localizes the impacts of replacing clear
 231 members with cloudy members (or *vice versa*). As an example, suppose the BGenKF re-
 232 places a cloudy forecast member with a clear analysis member. The localization process
 233 [Eq. (7)] first computes the difference between the cloudy forecast member and the clear
 234 analysis member (*i.e.*, the member's change due to the BGenKF). This difference is then lo-
 235 calized and applied to the cloudy forecast member. The resulting member follows the clear
 236 analysis member at the observation site and becomes increasingly like the cloudy forecast
 237 member with increasing distance from the observation site. Future work can examine other
 238 approaches to localize the impacts of deleting and replacing ensemble members.

239 **2.5.2 Handling overly small clusters**

240 The second heuristic sampling error mitigation measure is to switch from using the
 241 BGenKF to using the EnKF whenever the pre-resampling expanding cluster is too small
 242 ($N_{\text{pre}} < 0.8N_E$), or whenever any cluster is too small (less than $0.1N_E$). A similar heuristic
 243 measure is used in CAC20.

244 **2.5.3 Mitigating unphysical weight updates**

245 Another issue specific to the BGenKF is its occasional tendency to generate unphys-
 246 ical weight updates. Specifically, the BGenKF occasionally expands the clear cluster when
 247 a cloudy observation is assimilated, and *vice versa*. This is because the BGenKF does not
 248 explicitly consider whether an observation is clear or cloudy when assimilating it.

249 The BGenKF is automatically switched to the EnKF whenever an unphysical weight
 250 update is detected. To do so, we first identify the whether the observation to be assimilated
 251 is definitively clear or cloudy. In the case of Window-BT values over tropical ocean, obser-
 252 vation values warmer than 290 K are definitively clear, and observation values cooler than
 253 280 K are definitively cloudy. If the observation is definitively clear, but the cloudy cluster is
 254 expanded by the BGenKF, or *vice versa*, the BGenKF will switch over to the EnKF.

255 **3 Materials and methods**

256 **3.1 Description of October 2011 tropical convection case**

257 The BGenKF was tested against the EnKF using a case of tropical convection over the
 258 equatorial Indian Ocean during the October 2011 MJO. This case is chosen because it can be
 259 reasonably replicated by regional WRF models (S. Wang et al., 2015; F. Zhang et al., 2017;
 260 Ying & Zhang, 2017; Fu et al., 2017; X. Chen, Pauluis, & Zhang, 2018; X. Chen & Zhang,
 261 2019; Ying & Zhang, 2018; Chan, Zhang, et al., 2020).

262 Our experiments are conducted over a three day period during the onset of this MJO
 263 event (15 October 2011 to 18 October 2011). Two persistent regions of enhanced convection
 264 (henceforth, "convective regions") are observed in the 4-km Global IR Dataset of Janowiak
 265 et al. (2001) [henceforth, the MERG dataset]. The first convective region (blue rectangle)
 266 occurs between 60 °E and 75 °E and persists beyond the three-day period. Westward propa-

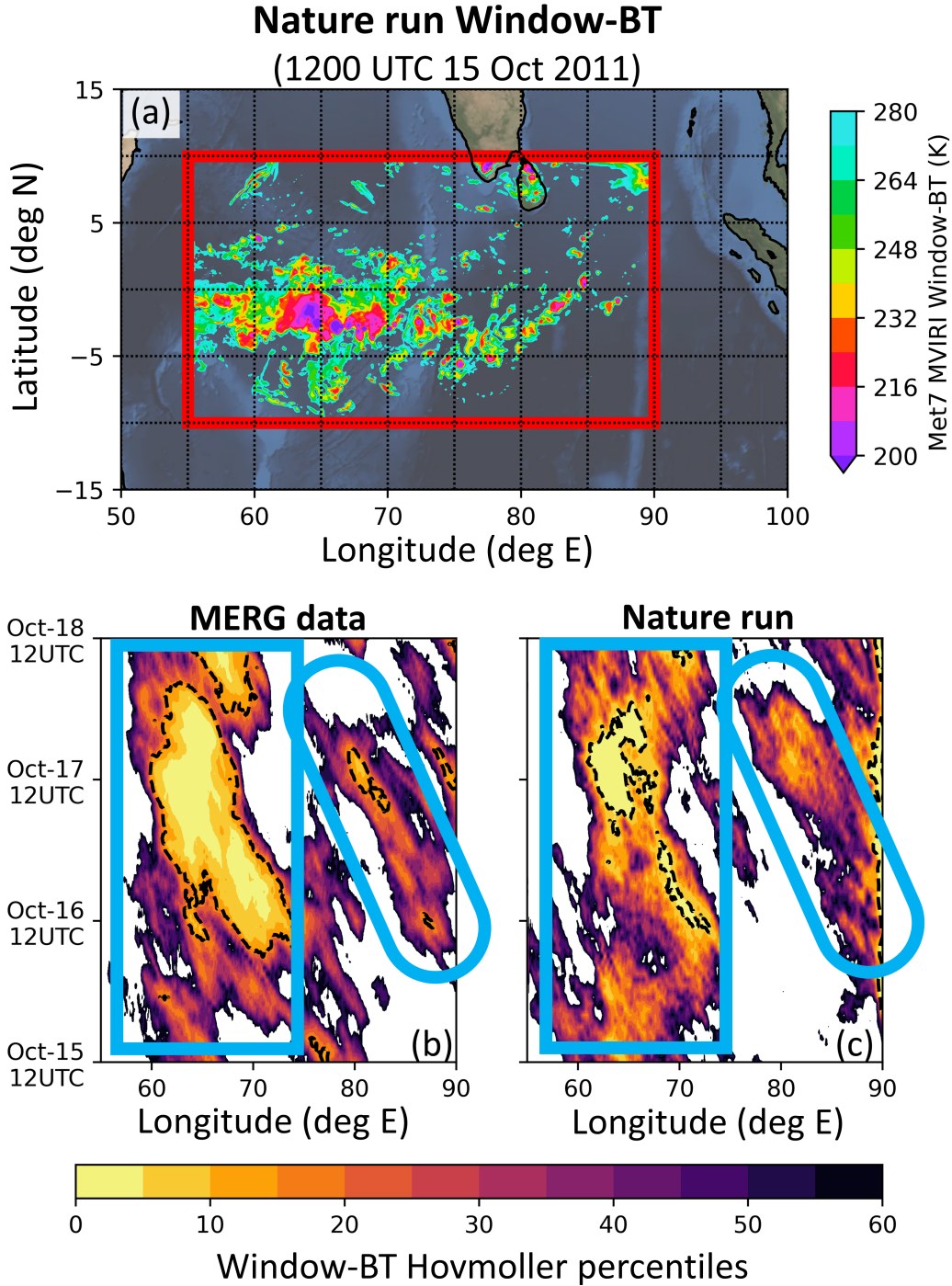


Figure 2. (a) Plot of our OSSE domain overlaid with the nature run’s simulated Window-BT field at 1200 UTC on 15th October 2011. The red box in panel (a) indicates our study domain. Also shown are longitude-time diagrams for the MERG dataset (b) and nature run (c). In panels (b) and (c), the shadings indicate Window-BT Hovmoller percentile values. These Window-BT Hovmoller percentile values are constructed by first averaging Window-BT values between between 10°S and 10°N at every hour to produce a time-longitude array of latitudinally-averaged Window-BT values. These arrays are then converted into percentiles before producing the longitude-time percentile values. Note that the dashed black contours in (b) and (c) indicate areas where the time-longitude arrays of latitudinally-averaged Window-BT values are below 260 K.

267 gation is observed in some of the clouds in this region, most notably between 1200 UTC on
 268 16 October and 0000 UTC on 18 October. The second convective region (blue oval) appears
 269 on the eastern edge of the study domain at 1200 UTC on 16th October and exhibits a west-
 270 ward propagation that is similar to that of the first system. We will later assess our OSSE's
 271 nature run simulation by checking the nature run against these two convective regions.

272 3.2 Setup of WRF model

273 The Advanced Research version of the WRF model (WRF-ARW) version 3.8 (Skamarock
 274 et al., 2008) is used in this study. Following Chan, Zhang, et al. (2020), we construct a 432×243
 275 WRF domain over the study domain [red box in Figure 2(a)] with 9-km horizontal grid spac-
 276 ing and 45 model levels. The bottommost 9 levels are within the lowest 1-km of the atmo-
 277 sphere and the pressure level at the top of the domain is set to 20 hPa. The WRF integration
 278 time step is set to 20 seconds.

279 Our WRF model setup uses the following parameterization schemes. Cloud micro-
 280 physical processes are handled by the WRF double-moment 6-class scheme (WDM6) pro-
 281 posed by Lim and Hong (2010). The updated Goddard shortwave scheme of Chou and Suarez
 282 (1999) and the Rapid Radiative Transfer Model (Global Circulation Model version; RRMTG)
 283 longwave scheme of Iacono et al. (2008) are used to parameterize radiative processes. The
 284 unified Noah land surface physics scheme (F. Chen & Dudhia, 2001) handles surface process
 285 and the Yonsei University (YSU) boundary layer scheme (Hong et al., 2006) is employed.
 286 No cumulus parameterization is employed because many studies have demonstrated that the
 287 9-km grid spacing is sufficient to resolve tropical mesoscale convective systems (MCS) over
 288 the region (S. Wang et al., 2015; Ying & Zhang, 2017, 2018; F. Zhang et al., 2017; X. Chen,
 289 Pauluis, & Zhang, 2018; X. Chen, Pauluis, Leung, & Zhang, 2018; X. Chen & Zhang, 2019;
 290 X. Chen et al., 2020; Chan, Zhang, et al., 2020; Chan & Chen, 2021; X. Chen, Leung, Feng,
 291 & Song, 2021; X. Chen, Leung, Feng, Song, & Yang, 2021; X. Chen et al., 2022).

292 3.3 Setup of WRF ensemble and nature run

293 This study's WRF ensemble and nature run are constructed by combining two datasets
 294 from the European Center for Medium-Range Forecasts (ECMWF): the ECMWF Reanalysis
 295 Version 5 [ERA5; Hersbach et al. (2020)] and the ECMWF's 50-member perturbed forecasts
 296 (Swinbank et al., 2016). The ERA5 dataset is downloaded for every hour between 0000 UTC
 297 on 15 October to 1800 UTC on 18 October from the ECMWF's Climate Data Store (CDS).
 298 The ECMWF's perturbed forecasts are produced as part of The Observing System Research
 299 and Predictability Experiment (THORPEX) Interactive Grand Global Ensemble [TIGGE;
 300 Swinbank et al. (2016)] and is downloaded for 0000 UTC on 15 October from the ECMWF's
 301 Meteorological Archival and Retrieval System (MARS).

302 The ERA5 and ECMWF's 50-member perturbed forecasts (TIGGE ensemble) are pro-
 303 cessed using the WRF Preprocessing System and WRF's real data processor (`real.exe`) to
 304 produce a set of 51 WRF initial conditions files. Note that the ERA5 is used to fill in the data
 305 missing from the TIGGE ensemble above 200 hPa. The 50 WRF initial conditions from the
 306 TIGGE ensemble are then recentered on the ERA5 WRF initial condition file. The end result
 307 is a 51-member ensemble of WRF initial conditions, where member 51 is based entirely on
 308 the ERA5 (*i.e.*, the 51-st ensemble perturbation is zero). Note that this 51-st member is not
 309 used to initialize the nature run. One of the other initial conditions is used to initialize the
 310 nature run.

311 The lower and lateral boundary conditions used in this study are based entirely on
 312 the hourly ERA5 dataset (*i.e.*, the boundary conditions are unperturbed). While perturbed
 313 boundary conditions can increase the ensemble spread, the ensemble spread is usually rea-
 314 sonable even with unperturbed boundary conditions (not shown). Furthermore, as a first
 315 approach to studying the potential impacts of the BGenKF in a high-order weather model

316 setting, we want the differences between the nature run (described later) and the OSSE en-
 317 semble to be entirely due to differences in the initial conditions. Future work can extend this
 318 study to situations with perturbed boundary conditions.

319 We desire a nature run that is roughly one ensemble standard deviation from our ex-
 320 periments' ensembles. To select an appropriate initial condition file for such a nature run,
 321 we first integrate the 51 members forward for 12 hours (from 0000 UTC to 1200 UTC on 15
 322 October 2011). This integration is performed to generate flow-dependent ensemble statis-
 323 tics that are consistent with the WRF model. After the 12-hour integration, we compute the
 324 following perturbation length metric (D^2) for each of the 51 ensemble members

$$D^2(n) \equiv \frac{1}{N_S N_i N_j} \sum_{v \in S} \sum_{i=1}^{N_i} \sum_{j=1}^{N_j} \left(\frac{\Lambda(i, j, v, n) - \langle \Lambda(i, j, v) \rangle_n}{\sigma_{i,j,v}} \right)^2. \quad (8)$$

325 $\Lambda(i, j, v, n)$ here is the value of a WRF-derived field v at horizontal index location (i, j) for
 326 ensemble member n . Furthermore, $\langle \Lambda(i, j, v) \rangle_n$ is the ensemble average of $\Lambda(i, j, v, n)$, and
 327 $\sigma_{i,j,v}$ is the ensemble standard deviation of $\Lambda(i, j, v, n)$. This means that the expression in
 328 the parentheses of Eq. (8) is the spread-normalized displacement of ensemble member n
 329 from the ensemble mean at location (i, j) for variable field v . The set S contains three 2D
 330 variables (precipitable water, column mass, and mass-integrated kinetic energy) and N_S is
 331 the size of the set S (*i.e.*, $N_S = 3$). Furthermore, N_i ($\equiv 432$) is the number of east-west grid
 332 points and N_j ($\equiv 243$) is the number of north-south grid points. The metric in Eq. (8) can
 333 thus be interpreted as being proportional to the spread-normalized Euclidean length of the
 334 n -th ensemble perturbation. As such, a D^2 value of unity means that the ensemble member is
 335 generally displaced from the ensemble mean by 1 standard deviation.

336 We define our nature run member to be the member whose D^2 value is closest to unity
 337 at 1200 UTC on 15 October. As a result, the nature run is based on member 10 of the TIGGE
 338 ensemble. The remaining 50 WRF members will be used for our cycling OSSE DA experi-
 339 ments.

340 3.4 Sanity check of nature run

341 Before proceeding, the nature run is checked by comparing it against the MERG dataset.
 342 Figure 2(b & c) shows longitude-time diagrams of the Window-BT percentiles from the
 343 MERG dataset and our nature run. The construction of these percentiles is explained in sec-
 344 tion 3.1 and in the caption of Figure 2.

345 We have opted to display the Window-BT percentiles instead of the Window-BT val-
 346 ues because the WRF model tends to under produce clouds (*i.e.*, when compared to satellite
 347 observations, the nature run Window-BTs are warm biased). This is illustrated by the dashed
 348 contours in Figure 2(b & c), which highlights areas where the latitudinally-averaged values
 349 of Window-BT were cooler than 260 K. These areas are substantially larger in the MERG
 350 data than in the nature run, meaning that the nature run under produced clouds. Since con-
 351 verting the Window-BT values to percentile values weakens the visual interference from the
 352 cloud biases, we have opted to display the Window-BT percentiles over the Window-BT val-
 353 ues.

354 Figure 2(c) indicates that the nature run also exhibits the two persistent convective re-
 355 gions observed in the MERG dataset (see section 3.1). These persistent convective regions
 356 are indicated by the blue rectangle and blue oval in Figure 2(c). Not only did the nature run's
 357 two persistent convective regions occur in locations and times similar to those of the MERG
 358 dataset (Figure 2(b)), these nature run regions also exhibit westward propagation patterns
 359 similar to those of the MERG dataset. As such, the nature run simulation reasonably repli-
 360 cates the anomalous convective behavior of the real atmosphere between 15 October to 18
 361 October 2011.

3.5 Setup of DA experiments to test the BGenKF

To test the BGenKF, three 50-member ensemble experiments are conducted. All three experiments start at 1200 UTC on 15 October and terminate at 1200 UTC on 18 October, with hourly DA cycling (73 cycles in total). The construction and spin-up of these 50 members are described in section 3.3.

In the first experiment, no observations are assimilated (henceforth, NoDA experiment). The NoDA experiment serves as a baseline for comparing the performance of the EnKF and BGenKF, and to measure imbalances induced by DA.

The other two experiments are the EnKF and BGenKF experiments. The only difference between the EnKF and BGenKF experiments is in the DA algorithm employed. The EnKF experiment will assimilate observations using the PSU-EnKF's (Meng & Zhang, 2007, 2008) default EnKF algorithm, and the BGenKF experiment will assimilate observations using a new implementation of the BGenKF into the PSU-EnKF. Note that both the EnKF and the BGenKF are implemented into the PSU-EnKF using the high-latency strategy proposed by Anderson and Collins (2007).

As a first approach to testing the BGenKF, only synthetic *Meteorological Satellite 7* (Meteosat Visible Infra-Red Imager (MVIRI) Window-BT observations will be assimilated. Future work can investigate if our findings can be extended to situations where an entire suite of operationally-assimilated observations and observations from different infrared channels are assimilated.

The synthetic Window-BT observations are constructed by first running the Community Radiative Transfer Model (CRTM) release 2.3.0 on the nature run (see sections 3.3 and 3.4). The nature run's Window-BT values are then thinned to a horizontal spacing of 27-km (~11,500 observations per DA cycle). White noise with a standard deviation of 3 K is then added to the thinned nature run Window-BT values to simulate instrument noise, thus constructing the synthetic observations. Note that the observation errors are likely to be correlated in reality. This means our use of white noise is an imperfect approximation to actual observation errors. Future work can investigate if our results can be extended to situations with correlated Window-BT observation errors.

Common heuristic strategies are employed to assimilate the Window-BT observations. To limit the impact of sampling errors, horizontal localization is applied using the Gaspari-Cohn fifth-order polynomial (Gaspari & Cohn, 1999) with a 100-km radius of influence (P. L. Houtekamer & Mitchell, 2001; Greybush et al., 2011; P. L. Houtekamer & Zhang, 2016). No vertical localization is employed. We also employ the Adaptive Observation Error Inflation scheme (AOEI) of Minamide and Zhang (2017) to limit the deleterious increments that can result from clear-cloudy disagreements between the prior and observations (F. Zhang et al., 2016; Minamide & Zhang, 2017). To mitigate the tendency for ensemble under-dispersion to occur when the ensemble is clear and the observation is cloudy, the Adaptive Background Error Inflation scheme (ABEI) of Minamide and Zhang (2019) is applied. We also employ 80% relaxation to prior perturbations (RTPP) to maintain ensemble dispersion (F. Zhang et al., 2004). Similar combinations of heuristic strategies are commonly seen in the EnKF-based DA of infrared radiance observations (F. Zhang et al., 2016; Minamide & Zhang, 2018; Chan, Zhang, et al., 2020; Y. Zhang et al., 2019; Chan & Chen, 2021; Y. Zhang et al., 2021).

Aside from these common strategies, we also restrict the BGenKF/EnKF from updating the domain-averaged specific humidity (QVAPOR) using Window-BT observations. Without this measure, both the BGenKF and the EnKF experience filter divergence that is related to DA-induced dry biases within 48 hours of cycling. These dry biases are likely induced by the ensemble's tendency to be overly cloudy. The dry biases in the EnKF experiment are likely partly because of the EnKF's inability to handle clear and cloudy members separately (see section 4.3). As for the BGenKF experiment, the dry bias can be explained

413 by the fact that the BGenKF algorithm frequently switches over to the EnKF algorithm
 414 (see section 4.2). Note that the BGenKF generated smaller dry biases than the EnKF (not
 415 shown).

416 To prevent filter divergence due to DA-induced dry biases, we replace the 3D posterior
 417 mean QVAPOR field ($\overline{q_v^a}$) with the following modified mean QVAPOR field ($\overline{q_v^*}$):

$$\overline{q_v^*}(i, j, k) \equiv \overline{q_v^a}(i, j, k) - \frac{1}{N_i N_j} \sum_{i=1}^{N_i} \sum_{j=1}^{N_j} \left\{ \overline{q_v^a}(i, j, k) - \overline{q_v^f}(i, j, k) \right\}. \quad (9)$$

418 Here, (i, j, k) refer to the west-east, south-north and bottom-top indices of the 3D QVAPOR
 419 fields and q_v^f refers to the 3D prior mean QVAPOR field.

420 3.6 Execution wall-time of the BGenKF

421 Before proceeding, we should compare the execution wall-time of the BGenKF and
 422 the EnKF. The BGenKF algorithm took ~30 seconds to assimilate ~11,500 observations us-
 423 ing 228 Intel Knight's Landing computer cores [distributed across 7 computational nodes on
 424 the National Energy Research Scientific Computing Center (NERSC) Cori supercomputer;
 425 each core has a clock rate of 1.4 GHz]. Assimilating the same observations via an EnKF al-
 426 gorithm took ~20 seconds of wall-time. For a fair comparison, this EnKF algorithm used
 427 the exact same code structure and computing resources, but with the cluster transfer and aux-
 428 iliary variable update steps disabled. In other words, the BGenKF used ~10 seconds more
 429 wall-time than the EnKF.

430 This ~10-second difference should be assessed in the context of the wall-time for the
 431 entire PSU-EnKF executable. The other components of the PSU-EnKF took ~100 seconds
 432 to execute. As such, the BGenKF only added ~10% wall-time to the entire PSU-EnKF exe-
 433 cutable. The BGenKF algorithm is thus likely affordable for research and operational groups
 434 that are already running serially-assimilating EnKFs [*e.g.*, Anderson et al. (2009)].

435 4 Perfect model WRF OSSE results

436 In the discussions to follow, we will be showing plots of normalized root-mean-square
 437 errors (nRMSEs) and normalized biases as functions of time and model level. The normal-
 438 ization is necessary for the ease of visualization, and uses the root-mean-square errors (RM-
 439 SEs) of the NoDA experiment. The EnKF experiment's nRMSE at model level k and date t
 440 is defined as

$$\text{EnKF nRMSE}(k, t) \equiv \frac{\text{EnKF RMSE}(k, t)}{\text{NoDA RMSE}(k, t)} \quad (10)$$

441 and likewise for that of the BGenKF and NoDA experiments (the NoDA's nRMSE values are
 442 always 1). Note that if a filter results in nRMSEs > 1.0, the assimilation of Window-BT via
 443 this filter degraded the ensemble with respect to the NoDA experiment. The reverse is true
 444 for nRMSEs < 1.0. We also define the normalized bias of the EnKF experiment to be

$$\text{EnKF normalized bias}(k, t) \equiv \frac{\text{EnKF bias}(k, t)}{\text{NoDA RMSE}(k, t)}, \quad (11)$$

445 and likewise for the BGenKF and NoDA experiments. These biases are computed by sub-
 446 tracting the nature run fields from the forecast ensemble mean fields.

447 The nRMSEs and normalized biases are examined for six variable fields: the zonal
 448 wind velocity component field (U), the meridional wind velocity component field (V), the
 449 temperature field (T), the QVAPOR field (Q), the Window-BT field, and the upper tropo-
 450 spheric infrared water vapor channel brightness temperature field (WV-BT; central wave-
 451 length of 6.2 μm). The nRMSEs are plotted in Figures 3 and 5(a & b) and the normalized bi-
 452 ases are plotted in Figures 4 and 5(c & d). All quantities are computed using forecast statis-
 453 tics.

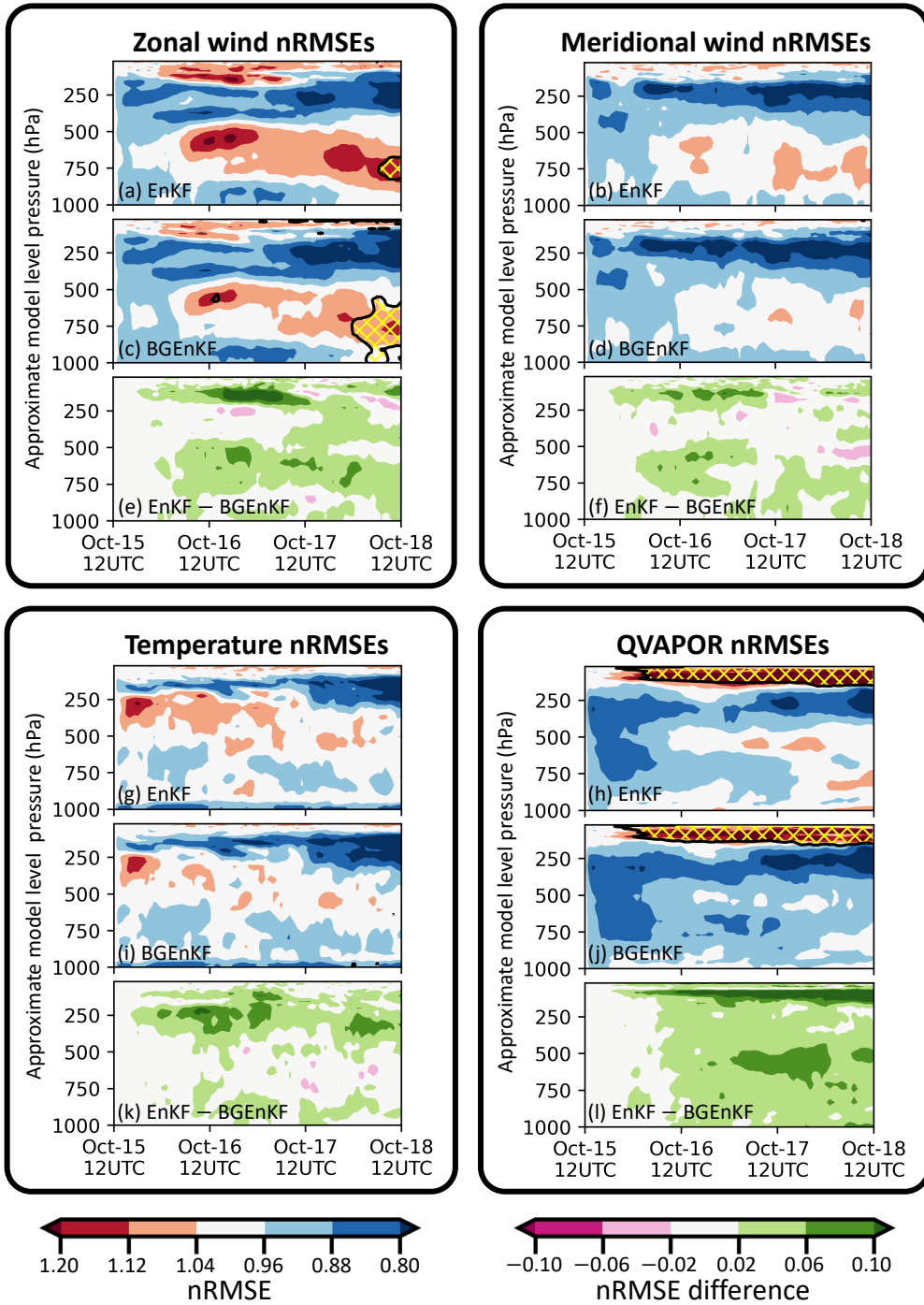


Figure 3. Plots of various prior ensemble statistics as functions of time and model level. For ease of interpretation, the model levels are displayed in terms of their approximate pressure levels (estimated using the definition of eta levels in WRF and assuming a surface pressure of 1000 hPa). The shadings indicate the NoDA-normalized RMSEs [nRMSEs; defined in Eq. (10)] for the EnKF (a, b, g & h) and BGenKF (c, d, i & j) experiments, as well as the nRMSE differences between the EnKF and BGenKF experiments (e, f, k & l). The nRMSEs and nRMSE differences are shown for the U field (a, c & e), V field (b, d & f), T field (g, i & k), and Q field (h, j & l). The areas outlined with a black contour and filled with yellow hatching have consistency ratios (spread/error) less than 0.75. Note that all displayed statistics are forecast statistics.

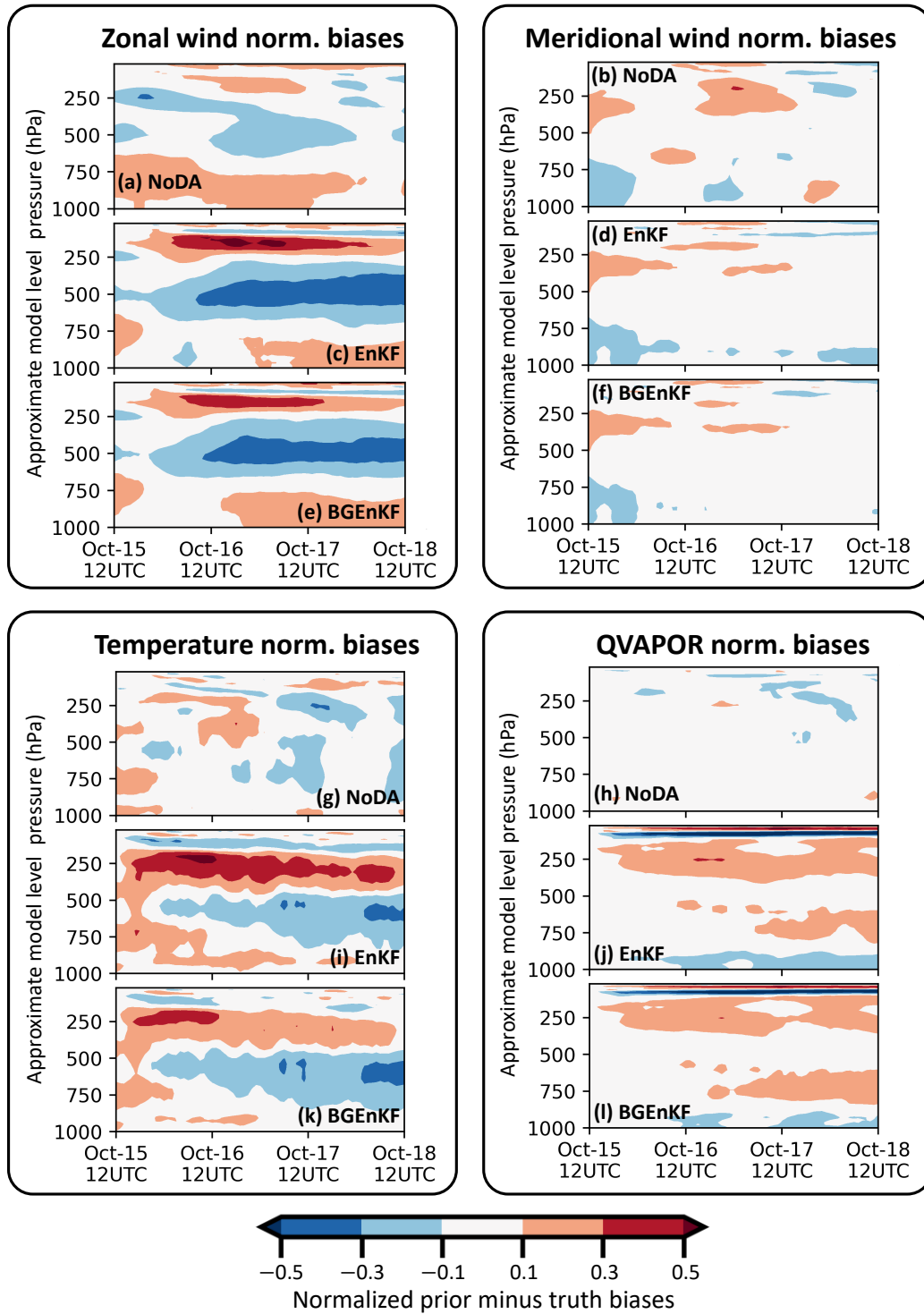


Figure 4. Plots of various prior ensemble normalized biases as functions of time and model level. These normalized biases are displayed for the U field (a, c & e), V field (b, d & f), T field (g, i & k), and Q field (h, j & l), for the NoDA (a, b, g & h), EnKF (c, d, i & j) and BGENKF (e, f, k & l) experiments. Similar to Figure 3, the model levels are displayed in terms of approximate pressure levels. See the Eq. (11) for the definition of the normalized biases.

4.1 On differences in the BGenKF's and the EnKF's performances during DA cycling

The nRMSEs and normalized biases of the BGenKF experiment are generally better than or comparable to those of the EnKF experiment (Figures 3 to 5). For the U, V, T and Q fields, subtracting the BGenKF's nRMSEs from the EnKF's nRMSEs generally results in positive values [Figure 3(e, f, k & l)]. The BGenKF experiment also has better WV-BT nRMSEs than the EnKF experiment [Figure 5(b)]. The BGenKF experiment also has smaller biases than the EnKF experiment in several places: the 100 hPa U field [Figure 4(c & e)], the 400–100 hPa T field [Figure 4(i & k)], the Window-BT field [Figure 5(e)], and WV-BT field [Figure 5(f)]. Otherwise, the BGenKF and EnKF experiments have similar bias values. These results suggest that the BGenKF is more suitable for assimilating all-sky Window-BT than the EnKF.

The BGenKF's performance advantages over the EnKF can be separated into two types. In the first type, the BGenKF generates larger improvements than the EnKF (*i.e.*, BGenKF nRMSEs < EnKF nRMSEs < NoDA nRMSEs). This type of performance advantage occurs in multiple places (Figures 3 and 5): 1) the 800 hPa to 1000 hPa U field nRMSEs during the first 56 cycles, 2) the 100 hPa to 500 hPa U field nRMSEs during the last 36 DA cycles, 3) the near surface and ~250 hPa V field nRMSEs from 0000 UTC on 16th October to 0000 UTC on 17th October, 4) between 100 hPa to 300 hPa in the T field nRMSEs for most cycles, 5) between 250 to 600 hPa in the Q field nRMSEs for most cycles, and in the WV-BT nRMSEs for most DA cycles after 0000 UTC on 16th October. These differences are likely due to the BGenKF's ability to handle mixture statistics, and suggest that the BGenKF is more suitable for assimilating Window-BT than the EnKF.

The BGenKF experiment's second type of performance advantage over the EnKF experiment is when the BGenKF introduces milder degradations than the EnKF (*i.e.*, NoDA nRMSEs < BGenKF nRMSEs < EnKF nRMSEs). In terms of nRMSEs (Figure 3), such situations are noticeable at the 100 hPa tropopause level and 500–700 hPa levels for the U and V fields, at the 200–500 hPa model levels for the T field, and at the 100 hPa level for the Q field. Such situations are also noticeable in the normalized biases of the ~100 hPa U field, the 100–400 hPa T field (Figure 4), and in the Window-BT and WV-BT fields (Figure 5). These are likely because 1) the BGenKF can handle mixture statistics whereas the EnKF cannot, and 2) the BGenKF experiment has smaller increments than the EnKF experiment because the BGenKF experiment has smaller dispersion. Figure 3(a & c) shows an example of the latter: the BGenKF U field has larger areas of low spread-to-error ratios (0.75) than the EnKF. The likely origins of the RMSE and bias degradations are discussed in section 4.2. Nonetheless, these results further support the notion that the BGenKF is more appropriate for assimilating Window-BT observations than the EnKF.

The BGenKF tends to result in smaller CRs than the EnKF because the BGenKF can outright convert all clear member columns to cloudy member columns, or *vice versa*. Since clear and cloudy member columns are very different, having both types of columns present at the same time boosts the ensemble spread. If all clear member columns are converted to cloudy member columns, or *vice versa*, large perturbations relative to the ensemble mean are replaced with smaller perturbations. This replacement results in reduced ensemble dispersion. Since the EnKF lacks this mechanism of ensemble spread removal, the BGenKF can remove more ensemble spread than the EnKF, thus resulting in smaller CRs than the EnKF. Future work can investigate if stronger inflation schemes are more appropriate for the BGenKF.

Note that there are occasional situations where the EnKF outperforms the BGenKF. For instance, at around 0000 UTC on 17th October the BGenKF's U nRMSEs are slightly higher than the EnKF at 250 hPa (Figure 3(e)). Other examples include the T nRMSEs around 1200 UTC on 17th October (Figure 3). Nonetheless, if we integrate the forecast ensembles'

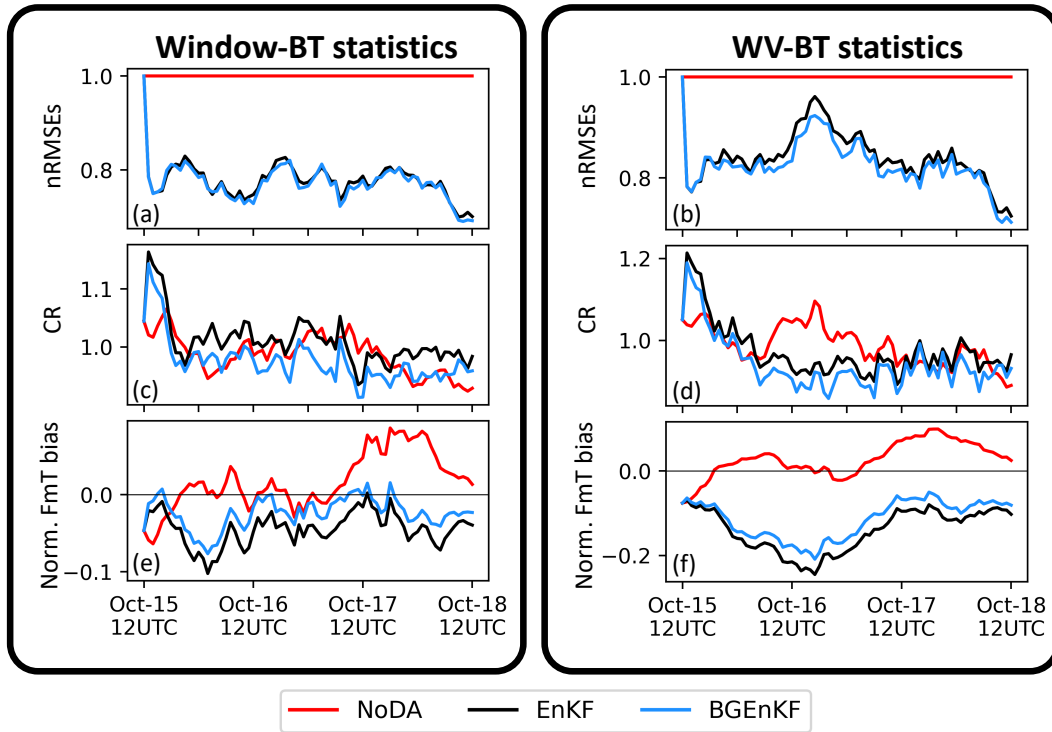


Figure 5. Time-series showing the performance statistics of the three experiments' prior ensembles in terms of Window-BT (a, c & e) and WV-BT (b, d & f). The definitions of nRMSEs (a & b) and normalized prior minus truth (Norm. FmT bias; e & f) are the same as in Figures 5 to 8. Like Figures 5 and 6, the consistency ratio (CR; c & d) here is defined as the ratio of spread to error.

505 nRMSEs with respect to pressure at every cycle, the resulting mass-weighted nRMSEs of the
 506 BGenKF experiment will be lower than those of the EnKF experiment.

507 We have also examined day-long deterministic forecasts that are initialized from the
 508 analysis means of the EnKF and BGenKF experiments (not shown). The BGenKF experi-
 509 ment's RMSE performance advantage over the EnKF experiment persists for up to 9 hours
 510 of lead time in terms of the U, V and T fields. In terms of the 500–800 hPa Q field RMSEs,
 511 the BGenKF experiment's RMSE advantage over the EnKF experiment persists throughout
 512 the 24 hours of integration. These results are as expected since the BGenKF experiment has
 513 lower RMSEs than the EnKF experiment during DA cycling.

514 **4.2 On the similar patterns observed in the performances of the BGenKF and** 515 **EnKF experiments**

516 Though the BGenKF experiment generally outperformed the EnKF experiment, there
 517 are common spatiotemporal patterns in their nRMSEs and normalized biases. For instance,
 518 Window-BT DA with either algorithm tends to degrade the 500–800 hPa U nRMSEs, and
 519 improve the 100–500 hPa U nRMSEs (Figure 3(a & c)). These similarities are likely because
 520 the BGenKF frequently switches over to the EnKF. Figure 6(a) shows that the BGenKF al-
 521 gorithm is only called to assimilate ~10% of the Window-BT observations, meaning that the
 522 switching occurred for the remaining ~90% of Window-BT observations. Future work can
 523 investigate if reducing the occurrence of such switches (*e.g.*, via weaker heuristic checks and
 524 larger ensembles) could improve the performance of the BGenKF.

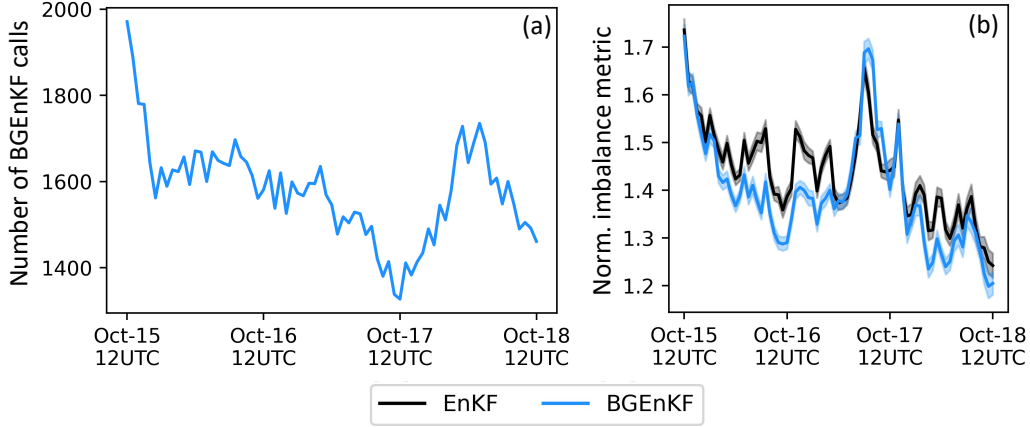


Figure 6. Plots showing the frequencies at which the two kernel BGenKF update procedure is called in the BGenKF experiment (a), and the normalized imbalance metric statistics for both the BGenKF and EnKF experiments (b). For reference, 11502 IR observations are assimilated at each DA cycle. The normalized imbalance metric is defined in the text. The solid curves in (b) indicate the ensemble average of every member’s normalized imbalance metric and the half-width of the shadings in (b) indicate twice the standard error of the members normalized imbalance metric.

525 It is notable that the BGenKF outperforms the EnKF despite the high frequency of
 526 BGenKF-to-EnKF switching. For instance, according to Figure 3(h, j & l), for the 24 cycles
 527 on 17th October and between 500 hPa to 700 hPa, the BGenKF experiment has 0.06–0.1 less
 528 Q nRMSEs than the EnKF experiment. Since the EnKF experiment has Q nRMSEs of ~1
 529 then, the BGenKF is able to introduce a ~6–10% improvement over the EnKF. These are
 530 considerable improvements since the BGenKF is only called on ~10% of the Window-BT
 531 observations.

532 Given the frequent switching from the BGenKF to the EnKF, the worse-than-NoDA
 533 RMSEs and biases in both the EnKF and BGenKF experiments are likely caused by the
 534 EnKF algorithm. These degradations are likely caused by 1) non-Gaussian forecast statis-
 535 tics, 2) sampling errors, and 3) biases that are introduced by the assimilation of Window-BT.
 536 The first factor can originate from having mixtures of clear and cloudy members. Sampling
 537 errors can also introduce errors into the analysis, particularly over regions where the ensem-
 538 ble correlations are weak. This factor is likely present in our experiments because no vertical
 539 localization is used in this study. Future work can investigate if vertical localization can mit-
 540 igate some of the RMSE and bias degradations (Lei & Anderson, 2014; Lei & Whitaker,
 541 2015; Lei et al., 2016, 2020). Finally, since biases are a component of RMSEs [e.g., Ying
 542 and Zhang (2017), Ying and Zhang (2018), and Chan, Zhang, et al. (2020)], biases that are
 543 introduced by Window-BT DA can contribute towards worse-than-NoDA RMSEs. While
 544 the contribution of biases to worse-than-NoDA RMSEs can be easily inferred (see the next
 545 paragraphs), the contributions from the first two factors cannot be easily teased apart.

To understand the contribution of biases to the occurrence of worse-than-NoDA RM-
 SEs (*i.e.*, nRMSEs > 1), we computed the following fraction as a function of model level and
 time ($f_{\text{bias}}(k, t)$). For the EnKF experiment, we defined

$$\text{EnKF's } f_{\text{bias}}(k, t) \equiv \sqrt{\frac{[\text{EnKF's biases}(k, t)]^2 - [\text{NoDA's biases}(k, t)]^2}{[\text{EnKF's RMSEs}(k, t)]^2 - [\text{NoDA's RMSEs}(k, t)]^2}}$$

546 and likewise for the BGenKF experiment. f_{bias} can be interpreted as the fractional contribu-
 547 tion of biases to the worse-than-NoDA RMSE performance.

We found that for about 25–45% of the worse-than-NoDA situations ($nRMSEs > 1$) in the U and T fields, the majority of the $nRMSE$ degradation (*i.e.*, $f_{bias} \geq 0.6$) can be explained by the the introduction of biases [*i.e.*, $p(f_{bias} > 0.6 | nRMSE > 1) \in (0.25, 0.45)$]. This suggests that though DA-induced biases are important contributors towards the worse-than-NoDA RMSEs of either DA filters, the net contribution coming from other factors is also important. Future work can examine separating and quantifying the relative importance of these three factors towards the worse-than-NoDA RMSEs.

4.3 On the origin of biases in the EnKF and BGenKF experiments

We now turn our attention to the U, T, Q, Window-BT and WV-BT biases that are introduced by Window-BT DA. Since the Q analysis increments are subject to bias removal (see last paragraph of section 3.5), the Q biases will be discussed later. The U, T and WV-BT biases are likely related to 1) a cold forecast minus truth (FmT) Window-BT bias at the start of all experiments, and 2) the persistence of these FmT Window-BT biases throughout all cycles (Figure 5(e)). Item 1 is essentially the result of drawing a single member from an ensemble – it is difficult to obtain a nature run whose domain-averaged Window-BT is always the same as that of the forecast ensemble. This is supported by the fact that the NoDA experiment’s FmT Window-BT biases oscillate around zero (Figure 5(e)). More interestingly, item 2 indicates an over abundance of clouds in both DA experiments. Since WV-BT is cooler in the presence of clouds, the WV-BT bias is explained by the over abundance of clouds.

To understand the origin of the persistently cold FmT Window-BT biases, we examine the analysis ensembles’ Window-BT biases. Running the CRTM on the analysis ensembles of the Window-BT DA experiments reveals analysis minus truth (AmT) Window-BT normalized biases that are typically around -0.25 (not shown). These bias values are a factor of 5 larger than the FmT normalized biases of around -0.05 (Figure 5(e)). The large AmT biases suggest that Window-BT DA resulted in overly cloudy analysis ensembles. Though the time-integration of these analysis ensembles dramatically reduces the over cloudiness (the normalized biases typically go from -0.25 to -0.05), some over cloudiness likely remain. As such, the U, T, Window-BT and WV-BT biases are likely caused by the EnKF and BGenKF experiments introducing too many clouds into the analysis ensemble.

The over introduction of clouds is likely a result of the EnKF’s inability to handle clear and cloudy members separately and the strong sensitivity of Window-BTs to hydrometeors. When both clear and cloudy members are present in the forecast ensemble, the EnKF’s forecast mean state will contain some amount of clouds. Suppose that the correlations between Window-BT and hydrometeor mixing ratios are negative. If Window-BT observations with either small or negative innovations are assimilated, the clouds in the EnKF’s mean state will either be unaffected (for small innovations) or be increased (for negative innovations). Since the EnKF will also reduce the size of the ensemble members’ perturbations, the ensemble thus contracts around a cloudy mean state. The result is that clear column forecast members gain some amount of clouds, even in situations where the innovations are close to zero. Since Window-BTs are sensitive to the presence of clouds, running the CRTM on such members will generate cold cloudy Window-BT values. This mechanism of EnKF-induced over-cloudiness warrants future investigation.

Note that the BGenKF experiment’s over-cloudiness is likely caused by the mechanism in the previous paragraph. This is because the BGenKF algorithm frequently switches over to the EnKF (for $\sim 90\%$ of assimilated observations). Since the BGenKF can handle mixtures of clear and cloudy members, with less frequent switches, the BGenKF is likely to have smaller biases. To test this possibility, smaller sampling errors are necessary to justify less frequent switches from the BGenKF to the EnKF. Future work can thus investigate this possibility with larger ensembles.

With regards to the Q biases, since the analysis increment cannot modify the Q biases [see Eq. (9)], these biases are induced during the forecast step of the DA procedure. We can

rule out the evaporation of DA-induced spurious clouds as an important source because the hydrometeor biases injected by the increment are an order of magnitude smaller than the Q bias growth during integration (not shown). Other processes are likely causing the Q biases. Some possibilities include enhancements to the upward transport of Q from the surface and/or the latent fluxes from the ocean surface. The exact origin of these Q biases can be investigated in future work.

4.4 On dynamical imbalances

Note that the BGenKF introduces less dynamical imbalances into the ensemble than the EnKF. To measure dynamical imbalance, we compute the root-mean-square of the second time derivative of surface pressure during the time integration phase of each DA cycle (P. Houtekamer & Mitchell, 2005; Temperton & Williamson, 1981). These derivatives are computed via centered differencing (Press & Flannery, 2010) on three consecutive snapshots of the surface pressure field. These snapshots are spaced 30-minutes apart. The resulting imbalance metric is normalized using the NoDA experiment's imbalance metric. A normalized imbalance metric value of 1 indicates that a normal amount of fast-moving gravity waves is present. A value greater than 1 indicates that a higher than normal amount of fast-moving gravity waves is present, thus indicating DA-induced imbalances.

Figure 6(b) indicates that the BGenKF experiment generally has either statistically indistinguishable or milder imbalances than the EnKF experiment. The only exception to this trend happens between 0000 UTC to 1200 UTC on 17th October. The BGenKF is thus likely more appropriate than the EnKF at assimilating Window-BT observations.

5 Conclusions and future work

In this study, we compare the BGenKF against the EnKF using perfect model OSSEs with a realistic weather model (WRF) for a case of tropical convection. These OSSEs are executed using the state-of-the-art PSU-EnKF system. Our results indicate that the BGenKF outperforms the EnKF at assimilating synthetic Window-BT observations. We observe this performance advantage in terms of the RMSEs and biases of the U, V, T, Q, Window-BT and WV-BT fields. This performance advantage is likely due to the BGenKF's ability to handle mixtures of clear and cloudy column members. These performance advantages are achieved even though the BGenKF is only activated for $\sim 10\%$ of the assimilated Window-BT observations. As such, these promising results motivate future work into the BGenKF using real data.

There are several large areas of future research for the BGenKF. The first large area concerns refining the BGenKF algorithm. Future work can, for instance, seek less heuristic approaches to sort the ensemble into clusters in a computationally efficient manner. One option is to combine clustering algorithms [*e.g.*, k-means (Forgy, 1965; Lloyd, 1982), support-vector machines (Cortes & Vapnik, 1995) and expectation maximization (Sondergaard & Lermusiaux, 2013b)] with dimension reduction methods [*e.g.*, Sondergaard and Lermusiaux (2013b), Reddy et al. (2020), Albarakati et al. (2021)]. Since cluster sizes, and thus sampling errors, can vary in each iteration of the serial BGenKF loop, future work can investigate using adaptive or empirical localization methods (Anderson, 2012; Anderson & Lei, 2013; Lei & Anderson, 2014) to improve the BGenKF's performance. Future work can also examine more sophisticated methods to regulate when the BGenKF switches over to the EnKF (*e.g.*, using the Shapiro-Wilk test for normality).

Another area of future work is to hybridize the BGenKF with other DA algorithms. Hybridization with kernel filters (Anderson & Anderson, 1999; Hoteit et al., 2008; Stordal et al., 2011; Hoteit et al., 2012; Liu et al., 2016; Stordal & Karlsen, 2017; Kotsuki et al., 2022) can be achieved by assigning the clear cluster's covariance to clear member kernels and likewise for the cloudy member kernels. Existing ensemble-variational hybrid DA al-

gorithms (Hamill & Snyder, 2000; Lorenc, 2003; Buehner, 2005; X. Wang et al., 2007) can also be hybridized with the BGenKF. For instance, the BGenKF can replace the EnKF component of such methods. Hybridization with DA methods that employ transport methods to update ensemble members (Reich, 2012; van Leeuwen, 2011; Marzouk et al., 2017; Hu & van Leeuwen, 2021; Evensen Geir et al., 2022) is also possible. This can provide a different method to shift members between clusters, as opposed to the current deletion-resampling method. Finally, the BGenKF can be potentially hybridized with ensemble DA methods that allow non-parametric prior distributions. Such methods include particle filters (van Leeuwen, 2009; Poterjoy, 2016; Vetra-Carvalho et al., 2018; Poterjoy et al., 2019; van Leeuwen et al., 2019), the quantile conserving ensemble filter (Anderson, 2022), and the rank histogram filter (Anderson, 2010, 2019, 2020).

Since we have only tested the BGenKF in a perfect model WRF OSSE using Window-BT observations, future work can test the BGenKF in increasingly realistic scenarios, with other observation types, and/or in other Earth systems. For instance, since radar reflectivity observations are sensitive to the presence and absence of precipitation, the BGenKF can potentially be better at assimilating such observations. The performance of the BGenKF can also be compared with other popular DA algorithms in tests that assimilate the operational suite of atmospheric in-situ and remote observations. Imperfect model OSSEs and real data tests can also be done. The BGenKF can also be tested in other Earth system components.

This study is among the first to demonstrate the potential of the BGenKF with a high-order weather model. Our BGenKF is computationally efficient, scalable with parallelization, and likely straightforward to implement in existing serial EnKF DA systems. These algorithmic properties and our promising results motivate future research into developing, testing and applying the BGenKF, or similar GMM-EnKFs, for Earth systems DA.

6 Open Research

The data and software used in this study are either publicly available or available upon request. The WRF model software can be found on the National Center for Atmospheric Research's WRF website (<https://www.mmm.ucar.edu/weather-research-and-forecasting-model>). Our WRF ensemble is constructed using the ECMWF TIGGE data archived on the MARS system (<https://apps.ecmwf.int/datasets/data/tigge>) and the ERA5 data archived on the CDS system (<https://cds.climate.copernicus.eu>). The MERG data product is obtained from NASA's GES DISC (https://disc.gsfc.nasa.gov/datasets/GPM_MERGIR_1/summary). We have archived this study's experiments and a copy of the Fortran 90 BGenKF module on the Pennsylvania State University's Data Commons (<http://doi.org/10.26208/XV41-7N75>). The Fortran 90 source code of the PSU-EnKF system, including the implemented BGenKF, is available upon request.

Acknowledgments

This work is supported by the Office of Naval Research (ONR) Grant N00014-18-1-2517, the National Aeronautics and Space Administration (NASA) Grant 80NSSC22K0613, the National Center for Atmospheric Research (NCAR) Advanced Study Program Graduate Visitor Program (ASP GVP), and the Water Cycle and Climate Extremes Modeling (WACCEM) project. WACCEM is funded by the U.S. Department of Energy Office of Science Biological and Environmental Research, as part of the Regional and Global Climate Modeling program, and NCAR is sponsored by the National Science Foundation. Any opinions, findings, and conclusions or recommendations expressed in this publication are those of the authors and do not necessarily reflect the views of the National Science Foundation. Finally, the computations in this study are performed using the Texas Advanced Computing Center (TACC) Stampede2 supercomputer and the National Energy Research Scientific Comput-

696 ing Center (NERSC) Cori supercomputer. NERSC is a U.S. Department of Energy Office of
697 Science User Facility operated under Contract DE-AC02-05CH11231.

698 References

- 699 Albarakati, A., Budišić, M., Crocker, R., Glass-Klaiber, J., Iams, S., Maclean, J., . . .
700 Van Vleck, E. S. (2021). Model and data reduction for data assimilation: Particle fil-
701 ters employing projected forecasts and data with application to a shallow water model.
702 *Computers and Mathematics with Applications*. doi: 10.1016/j.camwa.2021.05.026
- 703 Anderson, J. L. (2003, 4). A Local Least Squares Framework for Ensemble Filtering.
704 *Monthly Weather Review*, 131(4), 634–642. Retrieved from [http://journals](http://journals.ametsoc.org/doi/10.1175/1520-0493(2003)131<0634:ALLSFF>2.0.CO;2)
705 [.ametsoc.org/doi/10.1175/1520-0493\(2003\)131<0634:ALLSFF>2.0.CO;2](http://journals.ametsoc.org/doi/10.1175/1520-0493(2003)131<0634:ALLSFF>2.0.CO;2)
706 doi: 10.1175/1520-0493(2003)131<0634:ALLSFF>2.0.CO;2
- 707 Anderson, J. L. (2010, 11). A Non-Gaussian Ensemble Filter Update for Data Assimilation.
708 *Monthly Weather Review*, 138(11), 4186–4198. Retrieved from [http://journals](http://journals.ametsoc.org/doi/10.1175/2010MWR3253.1)
709 [.ametsoc.org/doi/10.1175/2010MWR3253.1](http://journals.ametsoc.org/doi/10.1175/2010MWR3253.1) doi: 10.1175/2010MWR3253.1
- 710 Anderson, J. L. (2012). Localization and sampling error correction in ensemble Kalman
711 filter data assimilation. *Monthly Weather Review*, 140(7). doi: 10.1175/MWR-D-11
712 -00013.1
- 713 Anderson, J. L. (2019). *A nonlinear rank regression method for ensemble Kalman filter data*
714 *assimilation* (Vol. 147) (No. 8). doi: 10.1175/MWR-D-18-0448.1
- 715 Anderson, J. L. (2020). A marginal adjustment rank histogram filter for non-Gaussian
716 ensemble data assimilation. *Monthly Weather Review*, 148(8). doi: 10.1175/
717 MWR-D-19-0307.1
- 718 Anderson, J. L. (2022). A Quantile-Conserving Ensemble Filter Framework. Part I: Updating
719 an Observed Variable. *Monthly Weather Review*, 150(5). doi: 10.1175/mwr-d-21-0229
720 .1
- 721 Anderson, J. L., & Anderson, S. L. (1999). A Monte Carlo implementation of the nonlinear
722 filtering problem to produce ensemble assimilations and forecasts. *Monthly Weather*
723 *Review*. doi: 10.1175/1520-0493(1999)127<2741:AMCIOT>2.0.CO;2
- 724 Anderson, J. L., & Collins, N. (2007, 8). Scalable Implementations of Ensemble Filter Algo-
725 rithms for Data Assimilation. *Journal of Atmospheric and Oceanic Technology*, 24(8),
726 1452–1463. Retrieved from [https://journals.ametsoc.org/view/journals/](https://journals.ametsoc.org/view/journals/atot/24/8/jtech2049_1.xml)
727 [atot/24/8/jtech2049_1.xml](https://journals.ametsoc.org/view/journals/atot/24/8/jtech2049_1.xml) doi: 10.1175/JTECH2049.1
- 728 Anderson, J. L., Hoar, T., Raeder, K., Liu, H., Collins, N., Torn, R., & Avellano, A. (2009,
729 9). The data assimilation research testbed a community facility. *Bulletin of the Amer-*
730 *ican Meteorological Society*, 90(9), 1283–1296. Retrieved from [https://journals](https://journals.ametsoc.org/doi/10.1175/2009BAMS2618.1)
731 [.ametsoc.org/doi/10.1175/2009BAMS2618.1](https://journals.ametsoc.org/doi/10.1175/2009BAMS2618.1) doi: 10.1175/2009BAMS2618.1
- 732 Anderson, J. L., & Lei, L. (2013). Empirical localization of observation impact in ensemble
733 Kalman filters. *Monthly Weather Review*, 141(11). doi: 10.1175/MWR-D-12-00330
734 .1
- 735 Buehner, M. (2005). Ensemble-derived stationary and flow-dependent background-error
736 covariances: Evaluation in a quasi-operational NWP setting. *Quarterly Journal of the*
737 *Royal Meteorological Society*, 131(607). doi: 10.1256/qj.04.15
- 738 Burgers, G., Jan van Leeuwen, P., Evensen, G., Van Leeuwen, P. J., & Evensen, G. (1998,
739 6). Analysis scheme in the ensemble Kalman filter. *Monthly Weather Review*, 126(6),
740 1719–1724. Retrieved from [http://journals.ametsoc.org/doi/10.1175/1520-](http://journals.ametsoc.org/doi/10.1175/1520-0493(1998)126<1719:ASITEK>2.0.CO;2)
741 [0493\(1998\)126<1719:ASITEK>2.0.CO;2](http://journals.ametsoc.org/doi/10.1175/1520-0493(1998)126<1719:ASITEK>2.0.CO;2) doi: 10.1175/1520-0493(1998)
742 126<1719:ASITEK>2.0.CO;2
- 743 Chan, M.-Y., Anderson, J. L., & Chen, X. (2020). An efficient bi-Gaussian ensemble Kalman
744 filter for satellite infrared radiance data assimilation. *Monthly Weather Review*. doi:
745 10.1175/mwr-d-20-0142.1
- 746 Chan, M.-Y., & Chen, X. (2021). Improving Analyses and Forecasts of a Tropical Squall
747 Line using Upper Tropospheric Infrared Satellite Observations. *Advances in Atmo-*
748 *spheric Sciences, Accepted Manuscript*. Retrieved from <http://www.iapjournals>

- 749 .ac.cn/aas/en/article/doi/10.1007/s00376-021-0449-8<http://www>
750 .iapjournals.ac.cn/aas/en/article/doi/10.1007/s00376-021-0449-8
751 ?viewType=HTML doi: 10.1007/S00376-021-0449-8
- 752 Chan, M.-Y., Zhang, F., Chen, X., & Leung, L. R. (2020). Potential Impacts of Assimilating
753 All-sky Satellite Infrared Radiances on Convection-Permitting Analysis and Prediction
754 of Tropical Convection. *Monthly Weather Review*. doi: 10.1175/mwr-d-19-0343.1
- 755 Chen, F., & Dudhia, J. (2001). Coupling and advanced land surface-hydrology model
756 with the Penn State-NCAR MM5 modeling system. Part I: Model implementation
757 and sensitivity. *Monthly Weather Review*. doi: 10.1175/1520-0493(2001)129<0569:
758 CAALSH>2.0.CO;2
- 759 Chen, X., Leung, L. R., Feng, Z., & Song, F. (2021, 10). Crucial Role of Mesoscale Con-
760 vective Systems in the Vertical Mass, Water and Energy Transports of the South Asian
761 Summer Monsoon. *Journal of Climate*, -1(aop), 1–46. Retrieved from [https://](https://journals.ametsoc.org/view/journals/clim/aop/JCLI-D-21-0124.1/JCLI-D-21-0124.1.xml)
762 [journals.ametsoc.org/view/journals/clim/aop/JCLI-D-21-0124.1/](https://journals.ametsoc.org/view/journals/clim/aop/JCLI-D-21-0124.1/JCLI-D-21-0124.1.xml)
763 [JCLI-D-21-0124.1.xml](https://journals.ametsoc.org/view/journals/clim/aop/JCLI-D-21-0124.1/JCLI-D-21-0124.1.xml) doi: 10.1175/JCLI-D-21-0124.1
- 764 Chen, X., Leung, L. R., Feng, Z., Song, F., & Yang, Q. (2021, 9). Mesoscale Convec-
765 tive Systems Dominate the Energetics of the South Asian Summer Monsoon Onset.
766 *Geophysical Research Letters*, 48(17), e2021GL094873. Retrieved from [https://](https://onlinelibrary.wiley.com/doi/full/10.1029/2021GL094873)
767 onlinelibrary.wiley.com/doi/full/10.1029/2021GL094873[https://](https://onlinelibrary.wiley.com/doi/abs/10.1029/2021GL094873)
768 onlinelibrary.wiley.com/doi/abs/10.1029/2021GL094873[https://](https://agupubs.onlinelibrary.wiley.com/doi/10.1029/2021GL094873)
769 agupubs.onlinelibrary.wiley.com/doi/10.1029/2021GL094873 doi:
770 10.1029/2021GL094873
- 771 Chen, X., Leung, L. R., Feng, Z., & Yang, Q. (2022, 4). Precipitation-Moisture Coupling
772 Over Tropical Oceans: Sequential Roles of Shallow, Deep, and Mesoscale Convec-
773 tive Systems. *Geophysical Research Letters*, 49(7). Retrieved from [https://](https://onlinelibrary.wiley.com/doi/10.1029/2022GL097836)
774 onlinelibrary.wiley.com/doi/10.1029/2022GL097836 doi: 10.1029/
775 2022GL097836
- 776 Chen, X., Nystrom, R. G., Davis, C. A., & Zarzycki, C. M. (2020, 12). Dynamical Struc-
777 tures of Cross-Domain Forecast Error Covariance of a Simulated Tropical Cyclone in
778 a Convection-Permitting Coupled Atmosphere-Ocean Model. *Monthly Weather Re-*
779 *view*, 149(1), 41–63. Retrieved from [https://journals.ametsoc.org/view/](https://journals.ametsoc.org/view/journals/mwre/149/1/mwr-d-20-0116.1.xml)
780 journals/mwre/149/1/mwr-d-20-0116.1.xml doi: 10.1175/mwr-d-20-0116.1
- 781 Chen, X., Pauluis, O. M., Leung, L. R., & Zhang, F. (2018). Multiscale atmospheric over-
782 turning of the Indian summer monsoon as seen through isentropic analysis. *Journal of*
783 *the Atmospheric Sciences*. doi: 10.1175/JAS-D-18-0068.1
- 784 Chen, X., Pauluis, O. M., & Zhang, F. (2018). Atmospheric overturning across multiple
785 scales of an MJO event during the CINDY/DYNAMO campaign. *Journal of the Atmo-*
786 *spheric Sciences*. doi: 10.1175/JAS-D-17-0060.1
- 787 Chen, X., & Zhang, F. (2019). Relative Roles of Preconditioning Moistening and Global
788 Circumnavigating Mode on the MJO Convective Initiation During DYNAMO. *Geo-*
789 *physical Research Letters*. doi: 10.1029/2018GL080987
- 790 Chou, M.-D., & Suarez, M. J. (1999). A Solar Radiation Parameterization Atmospheric
791 Studies. *Technical Report Series on Global Modeling and Data Assimilation*.
- 792 Cortes, C., & Vapnik, V. (1995). Support-Vector Networks. *Machine Learning*, 20(3). doi:
793 10.1023/A:1022627411411
- 794 Dovera, L., & Della Rossa, E. (2011). Multimodal ensemble Kalman filtering using Gaussian
795 mixture models. *Computational Geosciences*, 15(2), 307–323. doi: 10.1007/s10596
796 -010-9205-3
- 797 Dowell, D. C., Alexander, C. R., James, E. P., Weygandt, S. S., Benjamin, S. G., Manikin,
798 G. S., . . . Alcott, T. I. (2022). The High-Resolution Rapid Refresh (HRRR): An
799 Hourly Updating Convection-Allowing Forecast Model. Part 1: Motivation and System
800 Description. *Weather and Forecasting*. Retrieved from [https://journals.ametsoc](https://journals.ametsoc.org/view/journals/wefo/aop/WAF-D-21-0151.1/WAF-D-21-0151.1.xml)
801 [.org/view/journals/wefo/aop/WAF-D-21-0151.1/WAF-D-21-0151.1.xml](https://journals/wefo/aop/WAF-D-21-0151.1/WAF-D-21-0151.1.xml)
802 doi: 10.1175/WAF-D-21-0151.1
- 803 ECMWF. (2016). IFS Documentation CY41R2 - Part I: Observations | ECMWF. In *Ifs doc-*

- 804 umentation cy41r2 (chap. 1). ECMWF. Retrieved from [https://www.ecmwf.int/](https://www.ecmwf.int/en/elibrary/16646-ifs-documentation-cy41r2-part-i-observations)
805 en/elibrary/16646-ifs-documentation-cy41r2-part-i-observations
806 Edwards, C. A., Moore, A. M., Hoteit, I., & Cornuelle, B. D. (2015). Regional ocean data
807 assimilation. *Annual Review of Marine Science*, 7. doi: 10.1146/annurev-marine-
808 -010814-015821
- 809 Emanuel, K. A. (1994). *Atmospheric Convection*.
- 810 Evensen, G. (1994). Sequential data assimilation with a nonlinear quasi-geostrophic
811 model using Monte Carlo methods to forecast error statistics. *Journal of Geo-*
812 *physical Research*, 99(C5), 10143–10162. Retrieved from [https://doi.org/](https://doi.org/10.1029/94JC00572)
813 [10.1029/94JC00572](https://doi.org/10.1029/94JC00572)<http://doi.wiley.com/10.1029/94JC00572> doi:
814 [10.1029/94JC00572](https://doi.org/10.1029/94JC00572)
- 815 Evensen Geir, Vossepoel Femke C., & van Leeuwen Peter Jan. (2022). Particle Flow
816 for a Quasi-Geostrophic Model. In *Data assimilation fundamentals: A unified for-*
817 *mulation of the state and parameter estimation problem* (pp. 199–206). Cham:
818 Springer International Publishing. Retrieved from [https://doi.org/10.1007/](https://doi.org/10.1007/978-3-030-96709-3_20)
819 [978-3-030-96709-3_20](https://doi.org/10.1007/978-3-030-96709-3_20) doi: 10.1007/978-3-030-96709-3{_}20
- 820 Forgy, E. W. (1965). Cluster analysis of multivariate data: efficiency versus interpretability
821 of classifications. *Biometrics*, 21(3).
- 822 Fu, J. X., Wang, W., Shinoda, T., Ren, H. L., & Jia, X. (2017). Toward Understanding the
823 Diverse Impacts of Air-Sea Interactions on MJO Simulations. *Journal of Geophysical*
824 *Research: Oceans*, 122(11). doi: 10.1002/2017JC013187
- 825 Gaspari, G., & Cohn, S. E. (1999, 1). Construction of correlation functions in two and three
826 dimensions. *Quarterly Journal of the Royal Meteorological Society*, 125(554), 723–
827 757. Retrieved from <http://doi.wiley.com/10.1002/qj.4971255417> doi:
828 [10.1256/smsqj.55416](https://doi.org/10.1256/smsqj.55416)
- 829 Geer, A. J., & Bauer, P. (2011, 10). Observation errors in all-sky data assimilation. *Quarterly*
830 *Journal of the Royal Meteorological Society*, 137(661), 2024–2037. Retrieved from
831 <http://doi.wiley.com/10.1002/qj.830> doi: 10.1002/qj.830
- 832 Geer, A. J., Lonitz, K., Weston, P., Kazumori, M., Okamoto, K., Zhu, Y., . . . Schraff, C.
833 (2018). All-sky satellite data assimilation at operational weather forecasting centres.
834 *Quarterly Journal of the Royal Meteorological Society*. doi: 10.1002/qj.3202
- 835 Greybush, S. J., Kalnay, E., Miyoshi, T., Ide, K., & Hunt, B. R. (2011). Balance and ensem-
836 ble Kalman filter localization techniques. *Monthly Weather Review*, 139(2), 511–522.
837 doi: 10.1175/2010MWR3328.1
- 838 Grimes, D. I., & Pardo-Igúzquiza, E. (2010). Geostatistical analysis of rainfall. *Geographical*
839 *Analysis*, 42(2). doi: 10.1111/j.1538-4632.2010.00787.x
- 840 Hamill, T. M., & Snyder, C. (2000). A hybrid ensemble Kalman filter-3D variational anal-
841 ysis scheme. *Monthly Weather Review*, 128(8 II). doi: 10.1175/1520-0493(2000)
842 128<2905:ahkefv>2.0.co;2
- 843 Harnisch, F., Weissmann, M., & Perriñez. (2016). Error model for the assimilation of cloud-
844 affected infrared satellite observations in an ensemble data assimilation system. *Quar-*
845 *terly Journal of the Royal Meteorological Society*. doi: 10.1002/qj.2776
- 846 Helmert, J., Şorman, A. , Montero, R. A., De Michele, C., de Rosnay, P., Dumont, M., . . .
847 Arslan, A. N. (2018). *Review of snow data assimilation methods for hydrological, land*
848 *surface, meteorological and climate models: Results from a COST hamosnow survey*
849 (Vol. 8) (No. 12). doi: 10.3390/geosciences8120489
- 850 Hersbach, H., Bell, B., Berrisford, P., Hirahara, S., Horányi, A., Muñoz-Sabater, J., . . . Thé-
851 paut, J. N. (2020). The ERA5 global reanalysis. *Quarterly Journal of the Royal*
852 *Meteorological Society*. doi: 10.1002/qj.3803
- 853 Honda, T., Miyoshi, T., Lien, G. Y., Nishizawa, S., Yoshida, R., Adachi, S. A., . . . Bessho,
854 K. (2018, 1). Assimilating all-sky Himawari-8 satellite infrared radiances: A case of
855 Typhoon Soudelor (2015). *Monthly Weather Review*, 146(1), 213–229. doi: 10.1175/
856 MWR-D-16-0357.1
- 857 Hong, S. Y., Noh, Y., & Dudhia, J. (2006). A new vertical diffusion package with an ex-
858 plicit treatment of entrainment processes. *Monthly Weather Review*. doi: 10.1175/

MWR3199.1

859
860
861
862
863
864
865
866
867
868
869
870
871
872
873
874
875
876
877
878
879
880
881
882
883
884
885
886
887
888
889
890
891
892
893
894
895
896
897
898
899
900
901
902
903
904
905
906
907
908
909
910
911
912
913

- Hoteit, I., Luo, X., & Pham, D.-T. (2012, 2). Particle Kalman Filtering: A Nonlinear Bayesian Framework for Ensemble Kalman Filters. *Monthly Weather Review*, *140*(2), 528–542. Retrieved from <https://journals.ametsoc.org/doi/10.1175/2011MWR3640.1> doi: 10.1175/2011MWR3640.1
- Hoteit, I., Pham, D. T., Triantafyllou, G., & Korres, G. (2008). A new approximate solution of the optimal nonlinear filter for data assimilation in meteorology and oceanography. *Monthly Weather Review*, *136*(1). doi: 10.1175/2007MWR1927.1
- Houtekamer, P., & Mitchell, H. L. (2005, 10). Ensemble Kalman filtering. *Quarterly Journal of the Royal Meteorological Society*, *131*(613), 3269–3289. doi: 10.1256/qj.05.135
- Houtekamer, P. L., & Mitchell, H. L. (1998). Data assimilation using an ensemble Kalman filter technique. *Monthly Weather Review*, *126*(3), 796–811. doi: 10.1175/1520-0493(1998)126<0796:DAUAEK>2.0.CO;2
- Houtekamer, P. L., & Mitchell, H. L. (2001). A sequential ensemble Kalman filter for atmospheric data assimilation. *Monthly Weather Review*, *129*(1), 123–137. doi: 10.1175/1520-0493(2001)129<0123:ASEKFF>2.0.CO;2
- Houtekamer, P. L., & Zhang, F. (2016). Review of the ensemble Kalman filter for atmospheric data assimilation. *Monthly Weather Review*, *144*(12), 4489–4532. doi: 10.1175/MWR-D-15-0440.1
- Hu, C. C., & van Leeuwen, P. J. (2021). A particle flow filter for high-dimensional system applications. *Quarterly Journal of the Royal Meteorological Society*, *147*(737). doi: 10.1002/qj.4028
- Hunt, B. R., Kostelich, E. J., & Szunyogh, I. (2007, 6). Efficient data assimilation for spatiotemporal chaos: A local ensemble transform Kalman filter. *Physica D: Nonlinear Phenomena*, *230*(1-2), 112–126. Retrieved from <https://linkinghub.elsevier.com/retrieve/pii/S0167278906004647> doi: 10.1016/j.physd.2006.11.008
- Iacono, M. J., Delamere, J. S., Mlawer, E. J., Shephard, M. W., Clough, S. A., & Collins, W. D. (2008). Radiative forcing by long-lived greenhouse gases: Calculations with the AER radiative transfer models. *Journal of Geophysical Research Atmospheres*. doi: 10.1029/2008JD009944
- Janowiak, J. E., Joyce, R. J., & Yarosh, Y. (2001). A real-time global half-hourly pixel-resolution infrared dataset and its applications. *Bulletin of the American Meteorological Society*, *82*(2). doi: 10.1175/1520-0477(2001)082<0205:ARTGHH>2.3.CO;2
- Johnson, R. H., Rickenbach, T. M., Rutledge, S. A., Ciesielski, P. E., & Schubert, W. H. (1999). Trimodal characteristics of Tropical convection. *Journal of Climate*, *12*(8 PART 1). doi: 10.1175/1520-0442(1999)012<2397:tcotc>2.0.co;2
- Keppenne, C. L., Rienecker, M. M., Kurkowski, N. P., & Adamec, D. A. (2005). Ensemble Kalman filter assimilation of temperature and altimeter data with bias correction and application to seasonal prediction. *Nonlinear Processes in Geophysics*, *12*(4). doi: 10.5194/npg-12-491-2005
- Kotsuki, S., Miyoshi, T., Kondo, K., & Potthast, R. (2022). A Local Particle Filter and Its Gaussian Mixture Extension Implemented with Minor Modifications to the LETKF. *Geoscientific Model Development Discussions*, *2022*, 1–38. Retrieved from <https://gmd.copernicus.org/preprints/gmd-2022-69/> doi: 10.5194/gmd-2022-69
- Lei, L., & Anderson, J. L. (2014). Comparisons of empirical localization techniques for serial ensemble kalman filters in a simple atmospheric general circulation model. *Monthly Weather Review*, *142*(2). doi: 10.1175/MWR-D-13-00152.1
- Lei, L., Anderson, J. L., & Whitaker, J. S. (2016). Localizing the impact of satellite radiance observations using a global group ensemble filter. *Journal of Advances in Modeling Earth Systems*, *8*(2). doi: 10.1002/2016MS000627
- Lei, L., & Whitaker, J. S. (2015). Model space localization is not always better than observation space localization for assimilation of satellite radiances. *Monthly Weather Review*, *143*(10). doi: 10.1175/MWR-D-14-00413.1
- Lei, L., Whitaker, J. S., Anderson, J. L., & Tan, Z. (2020). Adaptive Localization for Satellite Radiance Observations in an Ensemble Kalman Filter. *Journal of Advances in*

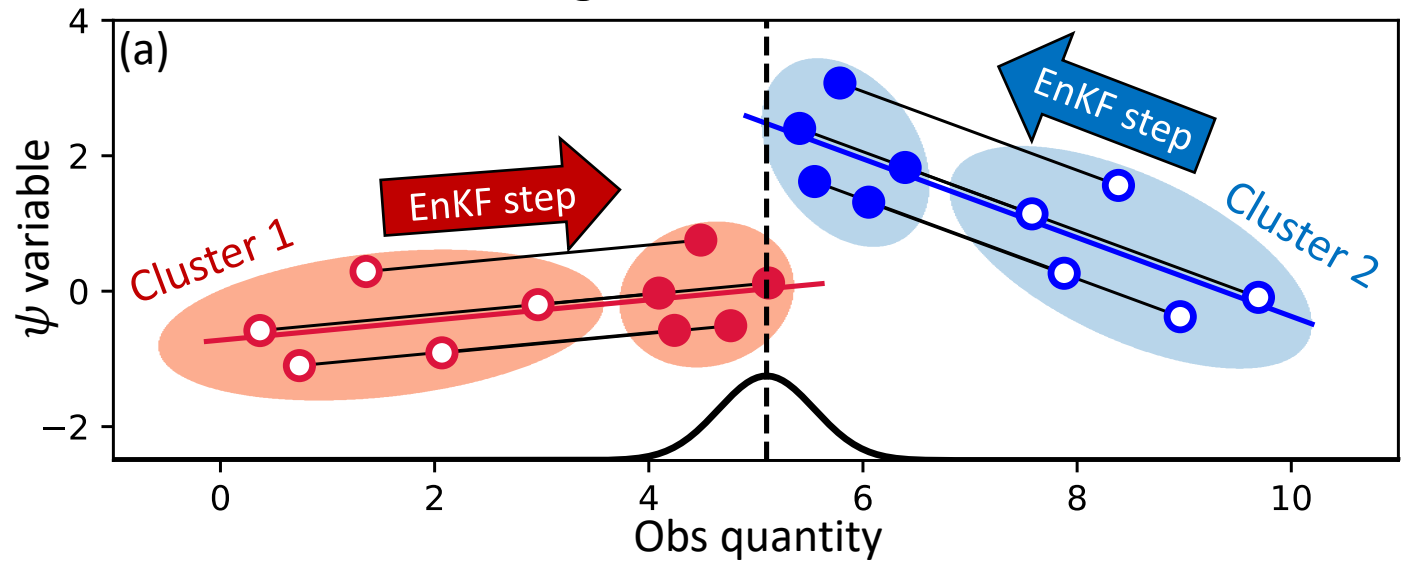
- 914 *Modeling Earth Systems*, 12(8). doi: 10.1029/2019MS001693
- 915 Lim, K. S. S., & Hong, S. Y. (2010). Development of an effective double-moment cloud
916 microphysics scheme with prognostic cloud condensation nuclei (CCN) for weather
917 and climate models. *Monthly Weather Review*. doi: 10.1175/2009MWR2968.1
- 918 Liu, B., Ait-El-Fquih, B., & Hoteit, I. (2016). Efficient kernel-based ensemble Gaussian
919 mixture filtering. *Monthly Weather Review*, 144(2). doi: 10.1175/MWR-D-14-00292
920 .1
- 921 Lloyd, S. P. (1982). Least Squares Quantization in PCM. *IEEE Transactions on Information
922 Theory*, 28(2). doi: 10.1109/TIT.1982.1056489
- 923 Lorenc, A. C. (2003). Modelling of error covariances by 4D-Var data assimilation. *Quarterly
924 Journal of the Royal Meteorological Society*, 129(595 PART B), 3167–3182. doi:
925 10.1256/qj.02.131
- 926 Madden, R. A., & Julian, P. R. (1971). Detection of a 40–50 Day Oscillation in the Zonal
927 Wind in the Tropical Pacific. *Journal of the Atmospheric Sciences*. doi: 10.1175/
928 1520-0469(1971)028<0702:doadoi>2.0.co;2
- 929 Madden, R. A., & Julian, P. R. (1972). Description of Global-Scale Circulation Cells in the
930 Tropics with a 40–50 Day Period. *Journal of the Atmospheric Sciences*. doi: 10.1175/
931 1520-0469(1972)029<1109:dogsc>2.0.co;2
- 932 Markowski, P., & Richardson, Y. (2010). *Mesoscale Meteorology in Midlatitudes*. doi:
933 10.1002/9780470682104
- 934 Marzouk, Y., Moselhy, T., Parno, M., & Spantini, A. (2017). Sampling via measure trans-
935 port: An introduction. In *Handbook of uncertainty quantification*. doi: 10.1007/
936 978-3-319-12385-1{_}23
- 937 Meng, Z., & Zhang, F. (2007). Tests of an ensemble Kalman filter for mesoscale and
938 regional-scale data assimilation. Part II: Imperfect model experiments. *Monthly
939 Weather Review*, 135(4), 1403–1423. doi: 10.1175/MWR3352.1
- 940 Meng, Z., & Zhang, F. (2008). Tests of an ensemble Kalman filter for mesoscale and
941 regional-scale data assimilation. Part III: Comparison with 3DVAR in a real-data case
942 study. *Monthly Weather Review*. doi: 10.1175/2007MWR2106.1
- 943 Minamide, M., & Zhang, F. (2017). Adaptive observation error inflation for assimilating
944 all-Sky satellite radiance. *Monthly Weather Review*, 145(3), 1063–1081. doi: 10.1175/
945 MWR-D-16-0257.1
- 946 Minamide, M., & Zhang, F. (2018). Assimilation of all-sky infrared radiances from
947 Himawari-8 and impacts of moisture and hydrometer initialization on convection-
948 permitting tropical cyclone prediction. *Monthly Weather Review*, 146(10), 3241–3258.
949 doi: 10.1175/MWR-D-17-0367.1
- 950 Minamide, M., & Zhang, F. (2019). An adaptive background error inflation method for
951 assimilating all-sky radiances. *Quarterly Journal of the Royal Meteorological Society*,
952 145(719), 805–823. doi: 10.1002/qj.3466
- 953 Park, S. K., & Xu, L. (2016). *Data assimilation for atmospheric, oceanic and hydrologic
954 applications (Vol. III)*. doi: 10.1007/978-3-319-43415-5
- 955 Poterjoy, J. (2016, 1). A localized particle filter for high-dimensional nonlinear sys-
956 tems. *Monthly Weather Review*, 144(1), 59–76. Retrieved from [http://journals](http://journals.ametsoc.org/doi/10.1175/MWR-D-15-0163.1)
957 [.ametsoc.org/doi/10.1175/MWR-D-15-0163.1](http://journals.ametsoc.org/doi/10.1175/MWR-D-15-0163.1) doi: 10.1175/MWR-D-15-0163
958 .1
- 959 Poterjoy, J., Wicker, L., & Buehner, M. (2019). Progress toward the application of a local-
960 ized particle filter for numerical weather prediction. *Monthly Weather Review*. doi:
961 10.1175/MWR-D-17-0344.1
- 962 Press, W., & Flannery, B. (2010). *Numerical Recipes in Fortran 90* (Vol. 35) (No. 6).
- 963 Reddy, G. T., Reddy, M. P. K., Lakshmana, K., Kaluri, R., Rajput, D. S., Srivastava, G., &
964 Baker, T. (2020). Analysis of Dimensionality Reduction Techniques on Big Data.
965 *IEEE Access*, 8. doi: 10.1109/ACCESS.2020.2980942
- 966 Reich, S. (2012). A Gaussian-mixture ensemble transform filter. *Quarterly Journal of the
967 Royal Meteorological Society*, 138(662). doi: 10.1002/qj.898
- 968 Reichle, R. H., Bosilovich, M. G., Crow, W. T., Koster, R. D., Kumar, S. V., Mahanama,

- 969 S. P. P., & Zaitchik, B. F. (2009). Recent Advances in Land Data Assimilation at
 970 the NASA Global Modeling and Assimilation Office. In *Data assimilation for atmo-*
 971 *spheric, oceanic and hydrologic applications*. doi: 10.1007/978-3-540-71056-1{\
 972 _}21
- 973 Skamarock, W., Klemp, J., Dudhi, J., Gill, D., Barker, D., Duda, M., . . . Powers, J.
 974 (2008). A Description of the Advanced Research WRF Version 3. NCAR Tech.
 975 Note NCAR/TN-468+STR, 113 pp. *NCAR TECHNICAL NOTE*. doi: 10.5065/
 976 D68S4MVH
- 977 Sondergaard, T., & Lermusiaux, P. F. (2013a). Data assimilation with gaussian mixture mod-
 978 els using the dynamically orthogonal field equations. Part II: Applications. *Monthly*
 979 *Weather Review*, *141*(6), 1761–1785. doi: 10.1175/MWR-D-11-00296.1
- 980 Sondergaard, T., & Lermusiaux, P. F. (2013b, 6). Data assimilation with gaussian mixture
 981 models using the dynamically orthogonal field equations. Part I: Theory and scheme.
 982 *Monthly Weather Review*, *141*(6), 1737–1760. Retrieved from [https://journals](https://journals.ametsoc.org/view/journals/mwre/141/6/mwr-d-11-00295.1.xml)
 983 [.ametsoc.org/view/journals/mwre/141/6/mwr-d-11-00295.1.xml](https://journals.ametsoc.org/view/journals/mwre/141/6/mwr-d-11-00295.1.xml) doi:
 984 10.1175/MWR-D-11-00295.1
- 985 Stammer, D., Balmaseda, M., Heimbach, P., Köhl, A., & Weaver, A. (2016). Ocean Data
 986 Assimilation in Support of Climate Applications: Status and Perspectives. *Annual*
 987 *Review of Marine Science*, *8*. doi: 10.1146/annurev-marine-122414-034113
- 988 Stordal, A. S., & Karlsen, H. A. (2017). Large sample properties of the adaptive gaussian
 989 mixture filter. *Monthly Weather Review*, *145*(7). doi: 10.1175/MWR-D-15-0372.1
- 990 Stordal, A. S., Karlsen, H. A., Nævdal, G., Skaug, H. J., & Vallès, B. (2011). Bridging
 991 the ensemble Kalman filter and particle filters: The adaptive Gaussian mixture filter.
 992 *Computational Geosciences*, *15*(2). doi: 10.1007/s10596-010-9207-1
- 993 Swinbank, R., Kyouda, M., Buchanan, P., Froude, L., Hamill, T. M., Hewson, T. D., . . . Ya-
 994 maguchi, M. (2016). The TIGGE project and its achievements. *Bulletin of the Ameri-*
 995 *can Meteorological Society*. doi: 10.1175/BAMS-D-13-00191.1
- 996 Temperton, C., & Williamson, D. L. (1981). Normal mode initialization for a multilevel
 997 grid-point model. Part I: Linear aspects. *Monthly Weather Review*, *109*(4). doi: 10
 998 .1175/1520-0493(1981)109<0729:NMIFAM>2.0.CO;2
- 999 Tippett, M. K., Anderson, J. L., Bishop, C. H., Hamill, T. M., & Whitaker, J. S. (2003, 7).
 1000 Ensemble Square Root Filters. *Monthly Weather Review*, *131*(7), 1485–1490. Re-
 1001 trieved from [http://journals.ametsoc.org/doi/10.1175/1520-0493\(2003\)](http://journals.ametsoc.org/doi/10.1175/1520-0493(2003)131%3C1485:ESRF%3E2.0.CO;2)
 1002 [131%3C1485:ESRF%3E2.0.CO;2](http://journals.ametsoc.org/doi/10.1175/1520-0493(2003)131%3C1485:ESRF%3E2.0.CO;2) doi: 10.1175/1520-0493(2003)131<1485:
 1003 ESRF>2.0.CO;2
- 1004 van Leeuwen, P. J. (2009). *Particle filtering in geophysical systems*. doi: 10.1175/
 1005 2009MWR2835.1
- 1006 van Leeuwen, P. J. (2011). Efficient nonlinear data assimilation for oceanic models of in-
 1007 termediate complexity. In *Ieee workshop on statistical signal processing proceedings*.
 1008 doi: 10.1109/SSP.2011.5967700
- 1009 van Leeuwen, P. J., Künsch, H. R., Nerger, L., Potthast, R., & Reich, S. (2019, 7). *Particle*
 1010 *filters for high-dimensional geoscience applications: A review* (Vol. 145) (No. 723).
 1011 John Wiley and Sons Ltd. doi: 10.1002/qj.3551
- 1012 Vetra-Carvalho, S., van Leeuwen, P. J., Nerger, L., Barth, A., Altaf, M. U., Brasseur, P., . . .
 1013 Beckers, J. M. (2018). State-of-the-art stochastic data assimilation methods for high-
 1014 dimensional non-Gaussian problems. *Tellus, Series A: Dynamic Meteorology and*
 1015 *Oceanography*. doi: 10.1080/16000870.2018.1445364
- 1016 Wang, S., Sobel, A. H., Zhang, F., Qiang Sun, Y., Yue, Y., & Zhou, L. (2015). Re-
 1017 gional simulation of the october and november MJO events observed during the
 1018 CINDY/DYNAMO field campaign at gray zone resolution. *Journal of Climate*, *28*(6),
 1019 2097–2119. doi: 10.1175/JCLI-D-14-00294.1
- 1020 Wang, X., Snyder, C., & Hamill, T. M. (2007). On the theoretical equivalence of differ-
 1021 ently proposed ensemble - 3DVAR hybrid analysis schemes. *Monthly Weather Review*,
 1022 *135*(1). doi: 10.1175/MWR3282.1
- 1023 Whitaker, J. S., & Hamill, T. M. (2002, 7). Ensemble data assimilation without perturbed

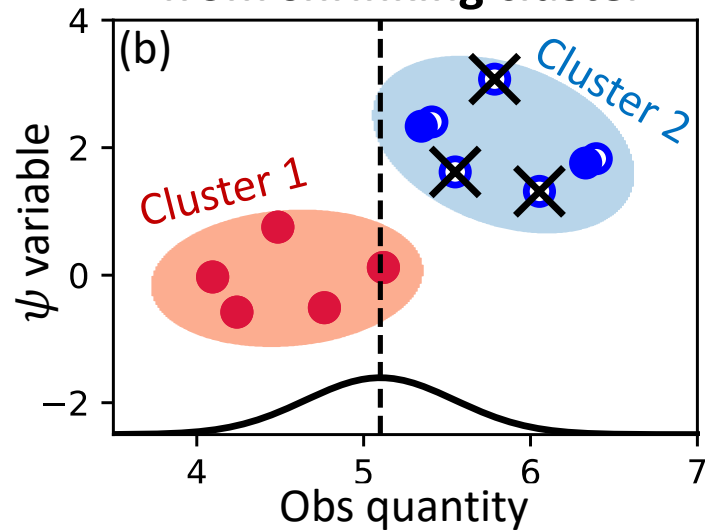
- 1024 observations. *Monthly Weather Review*, *130*(7), 1913–1924. Retrieved from [http://](http://journals.ametsoc.org/doi/10.1175/1520-0493(2002)130%3C1913:EDAWPO%3E2.0.CO;2)
 1025 [journals.ametsoc.org/doi/10.1175/1520-0493\(2002\)130%3C1913:EDAWPO%](http://journals.ametsoc.org/doi/10.1175/1520-0493(2002)130%3C1913:EDAWPO%3E2.0.CO;2)
 1026 [3E2.0.CO;2](http://journals.ametsoc.org/doi/10.1175/1520-0493(2002)130%3C1913:EDAWPO%3E2.0.CO;2) doi: 10.1175/1520-0493(2002)130<1913:EDAWPO>2.0.CO;2
- 1027 Whitaker, J. S., Hamill, T. M., Wei, X., Song, Y., & Toth, Z. (2008). Ensemble data assim-
 1028 ilation with the NCEP global forecast system. *Monthly Weather Review*, *136*(2). doi:
 1029 10.1175/2007MWR2018.1
- 1030 Ying, Y., & Zhang, F. (2017). Practical and intrinsic predictability of multiscale weather and
 1031 convectively coupled equatorial waves during the active phase of an MJO. *Journal of*
 1032 *the Atmospheric Sciences*, *74*(11), 3771–3785. doi: 10.1175/JAS-D-17-0157.1
- 1033 Ying, Y., & Zhang, F. (2018). Potentials in improving predictability of multiscale tropical
 1034 weather systems evaluated through ensemble assimilation of simulated satellite-based
 1035 observations. *Journal of the Atmospheric Sciences*, *75*(5), 1675–1698. doi: 10.1175/
 1036 JAS-D-17-0245.1
- 1037 Zhang, F., Minamide, M., & Clothiaux, E. E. (2016). Potential impacts of assimilating all-
 1038 sky infrared satellite radiances from GOES-R on convection-permitting analysis and
 1039 prediction of tropical cyclones. *Geophysical Research Letters*, *43*(6), 2954–2963. doi:
 1040 10.1002/2016GL068468
- 1041 Zhang, F., Snyder, C., & Sun, J. (2004, 5). Impacts of initial estimate and observation avail-
 1042 ability on convective-scale data assimilation with an ensemble Kalman filter. *Monthly*
 1043 *Weather Review*, *132*(5), 1238–1253. doi: 10.1175/1520-0493(2004)132<1238:
 1044 IOIEAO>2.0.CO;2
- 1045 Zhang, F., Taraphdar, S., & Wang, S. (2017). The role of global circumnavigating mode in
 1046 the MJO initiation and propagation. *Journal of Geophysical Research*, *122*(11), 5837–
 1047 5856. doi: 10.1002/2016JD025665
- 1048 Zhang, Y., Sieron, S. B., Lu, Y., Chen, X., Nystrom, R. G., Minamide, M., . . . Zhang, F.
 1049 (2021, 12). *Ensemble-Based Assimilation of Satellite All-Sky Microwave Radiances*
 1050 *Improves Intensity and Rainfall Predictions for Hurricane Harvey (2017)* (Vol. 48)
 1051 (No. 24). John Wiley and Sons Inc. doi: 10.1029/2021GL096410
- 1052 Zhang, Y., Stensrud, D. J., & Zhang, F. (2019, 12). Simultaneous Assimilation of Radar and
 1053 All-Sky Satellite Infrared Radiance Observations for Convection-Allowing Ensemble
 1054 Analysis and Prediction of Severe Thunderstorms. *Monthly Weather Review*, *147*(12),
 1055 4389–4409. Retrieved from [https://journals.ametsoc.org/view/journals/](https://journals.ametsoc.org/view/journals/mwre/147/12/mwr-d-19-0163.1.xml)
 1056 [mwre/147/12/mwr-d-19-0163.1.xml](https://journals.ametsoc.org/view/journals/mwre/147/12/mwr-d-19-0163.1.xml) doi: 10.1175/MWR-D-19-0163.1

Figure 1.

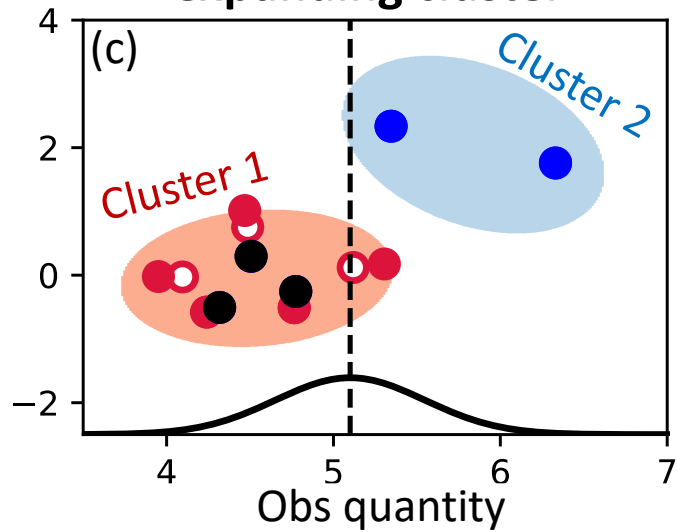
Stage 1: Double EnKF



Stage 2: Delete members from shrinking cluster



Stage 3: Resample expanding cluster



- Cluster 1 members (pre-stage)
- Cluster 1 members (post-stage)
- Cluster 1 regression line
- ✕ Delete member
- New member
- $p(y^o | \psi)$

- Cluster 2 members (pre-stage)
- Cluster 2 members (post-stage)
- Cluster 2 regression line
- EnKF increment
- - - Observation

Figure 6.

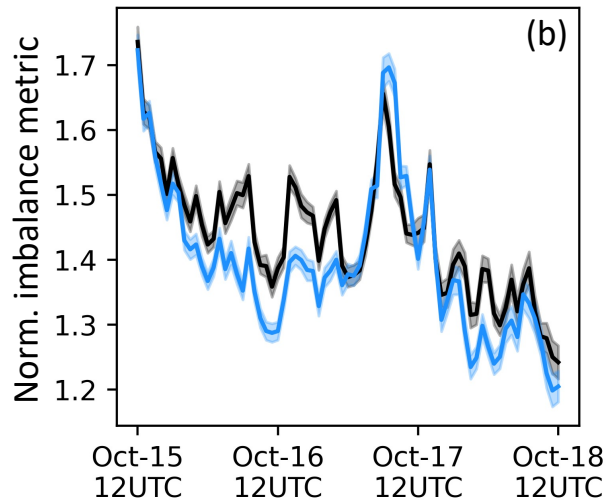
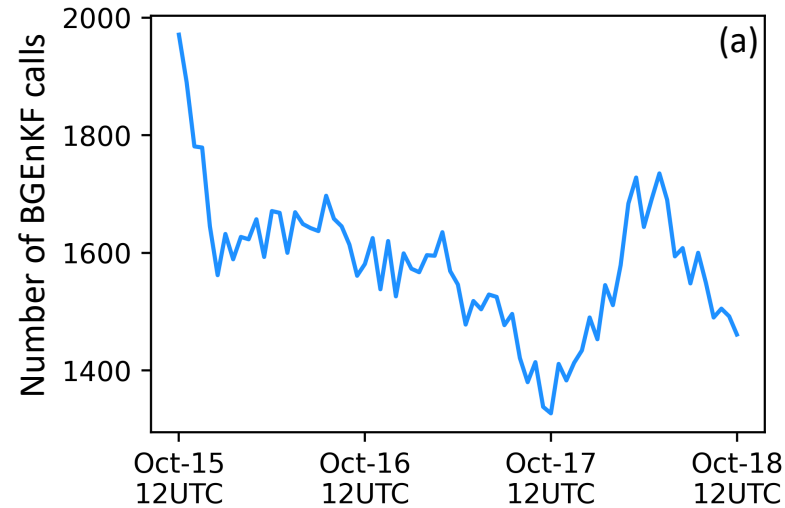
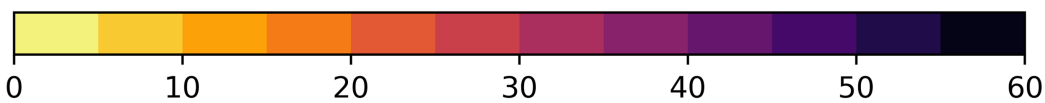
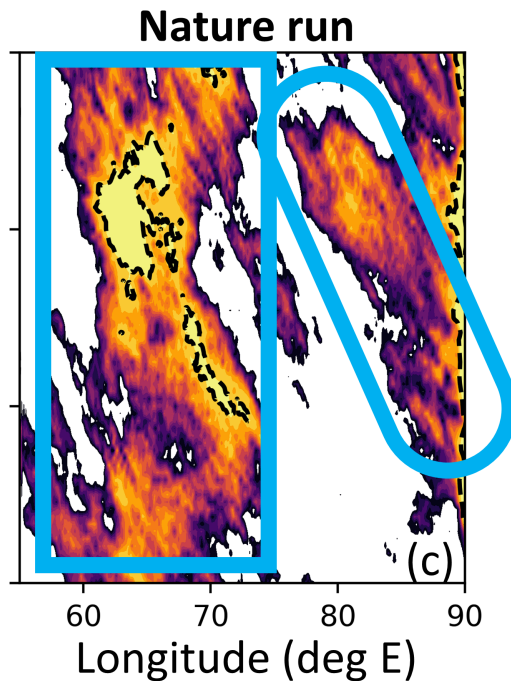
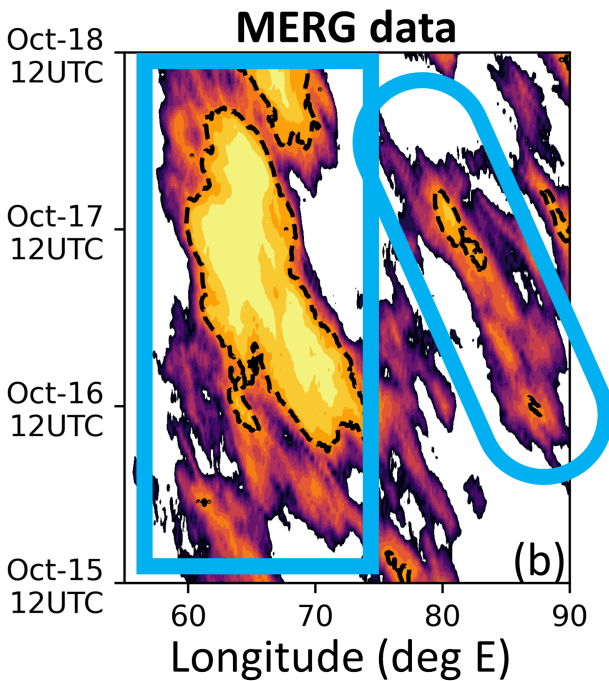
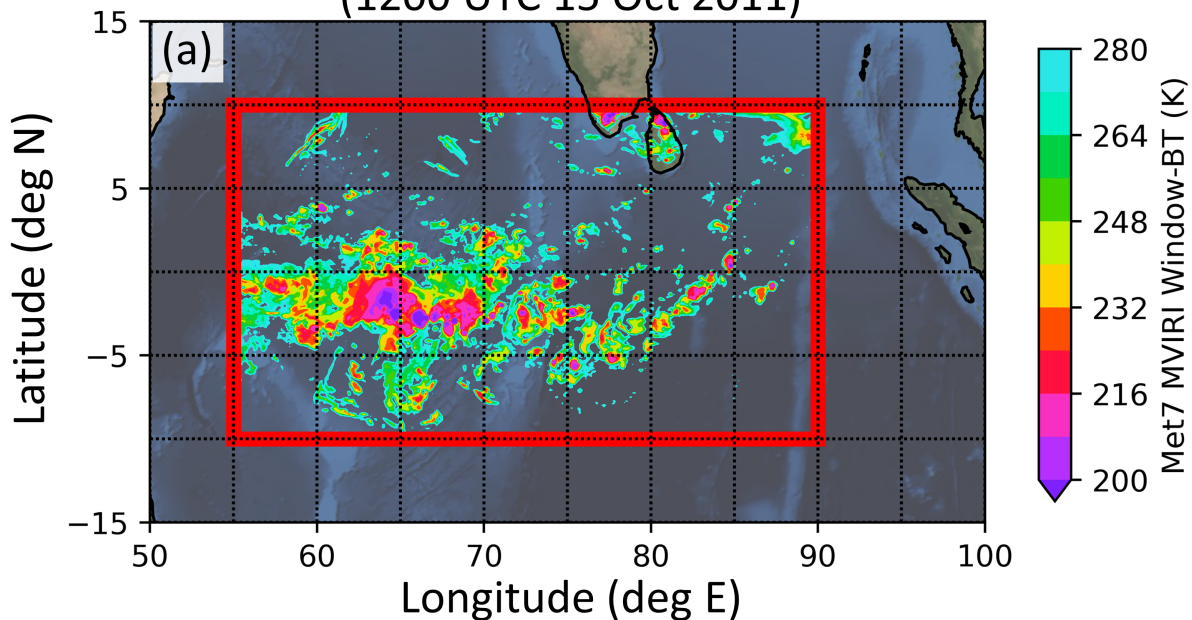


Figure 2.

Nature run Window-BT

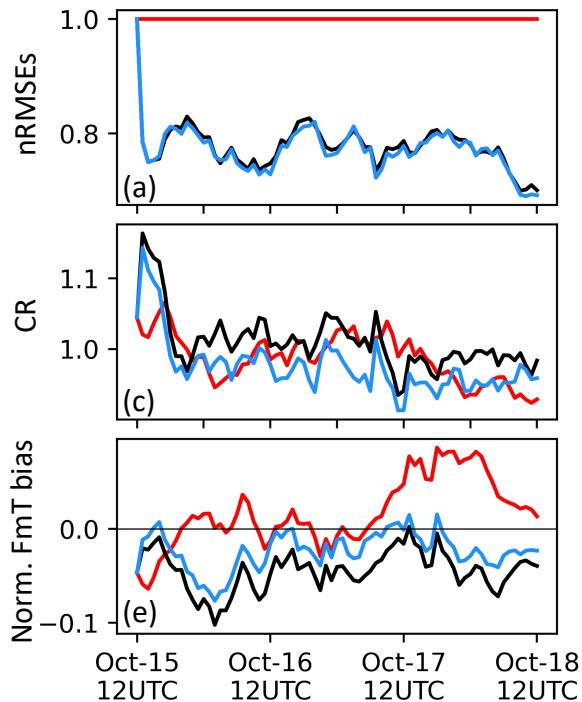
(1200 UTC 15 Oct 2011)



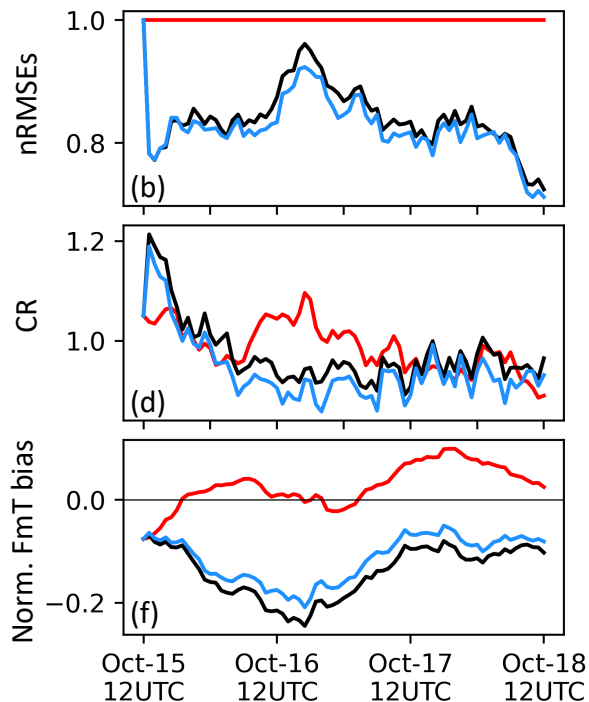
Window-BT Hovmoller percentiles

Figure 5.

Window-BT statistics



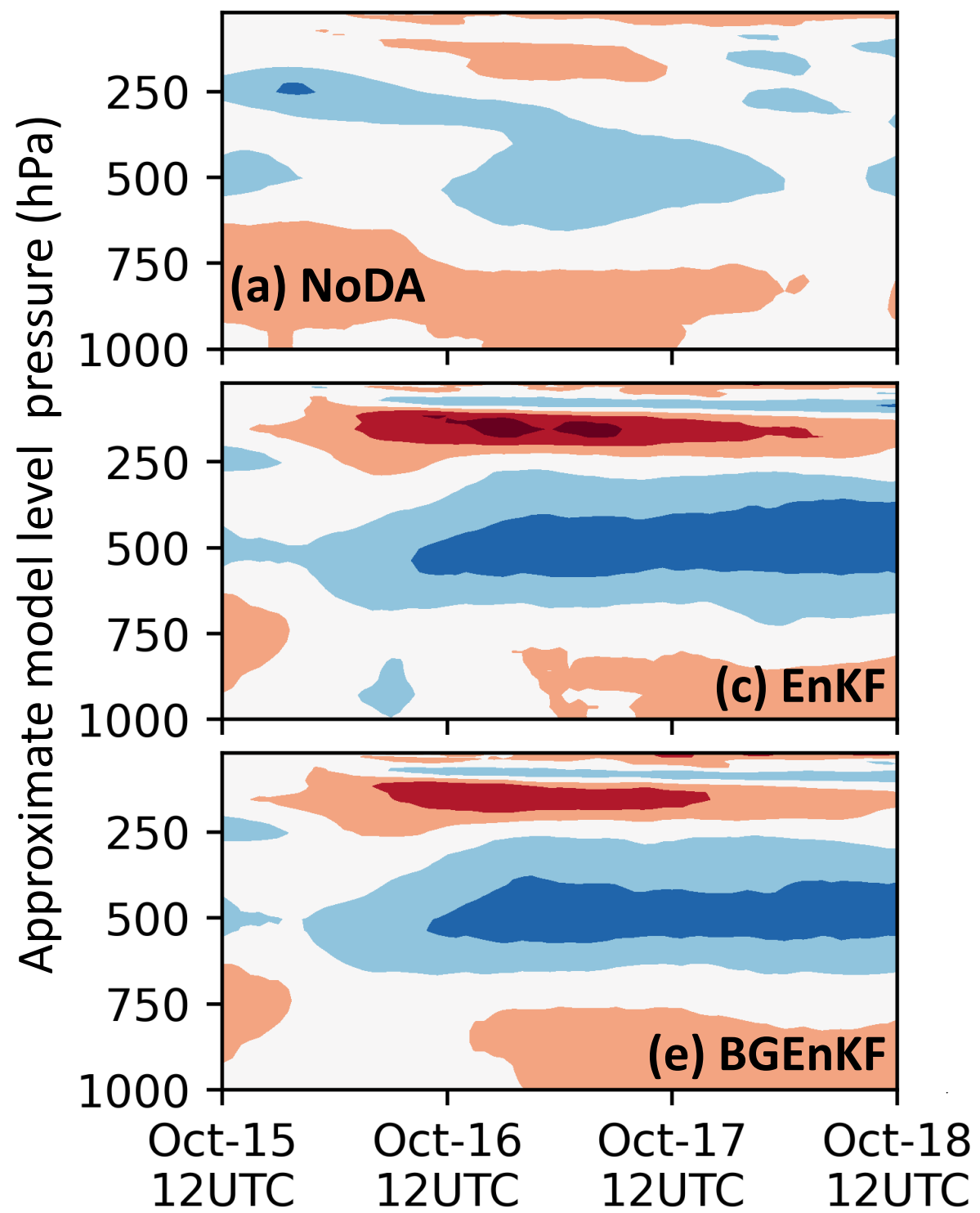
WV-BT statistics



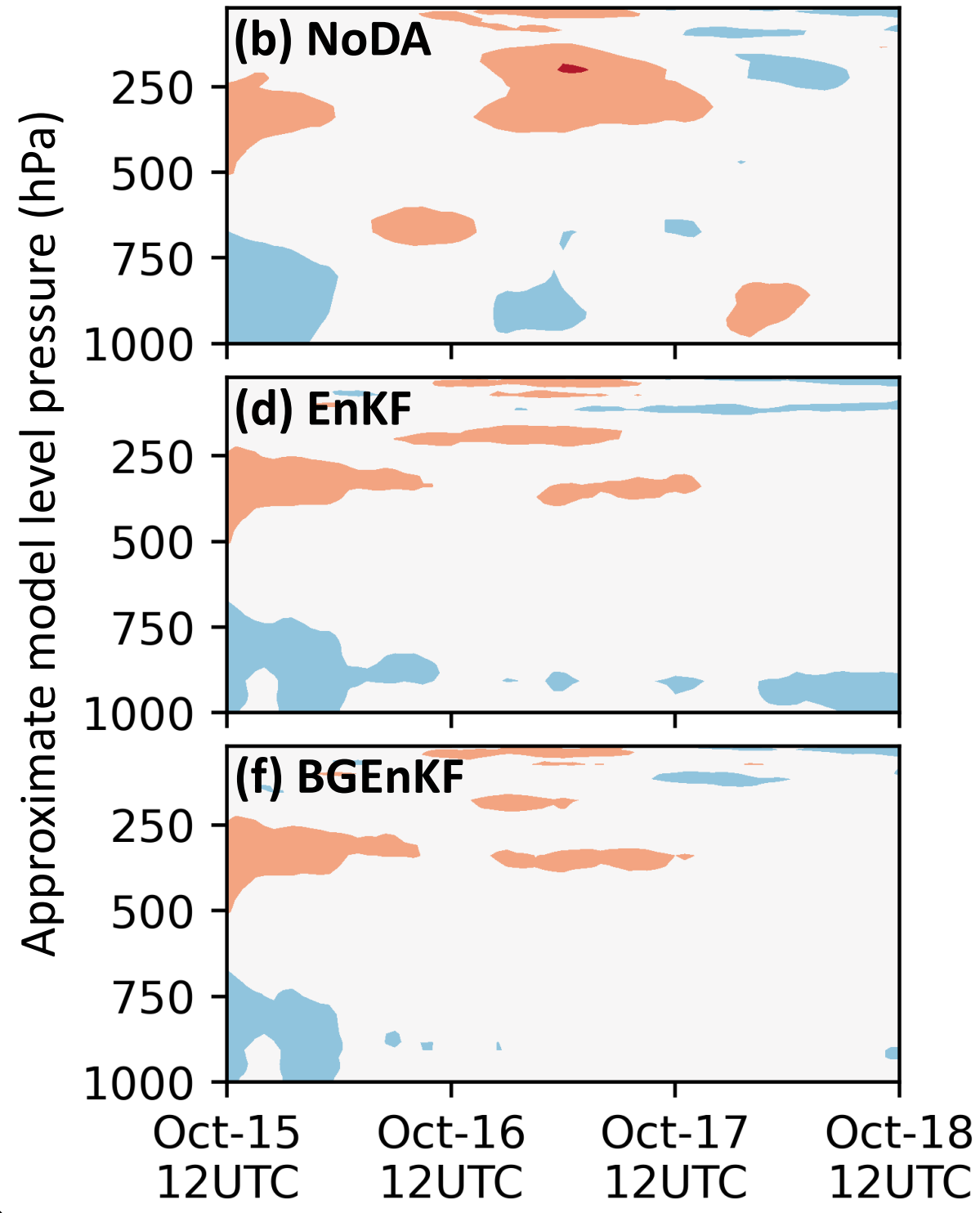
— NoDA — EnKF — BGenKF

Figure 4.

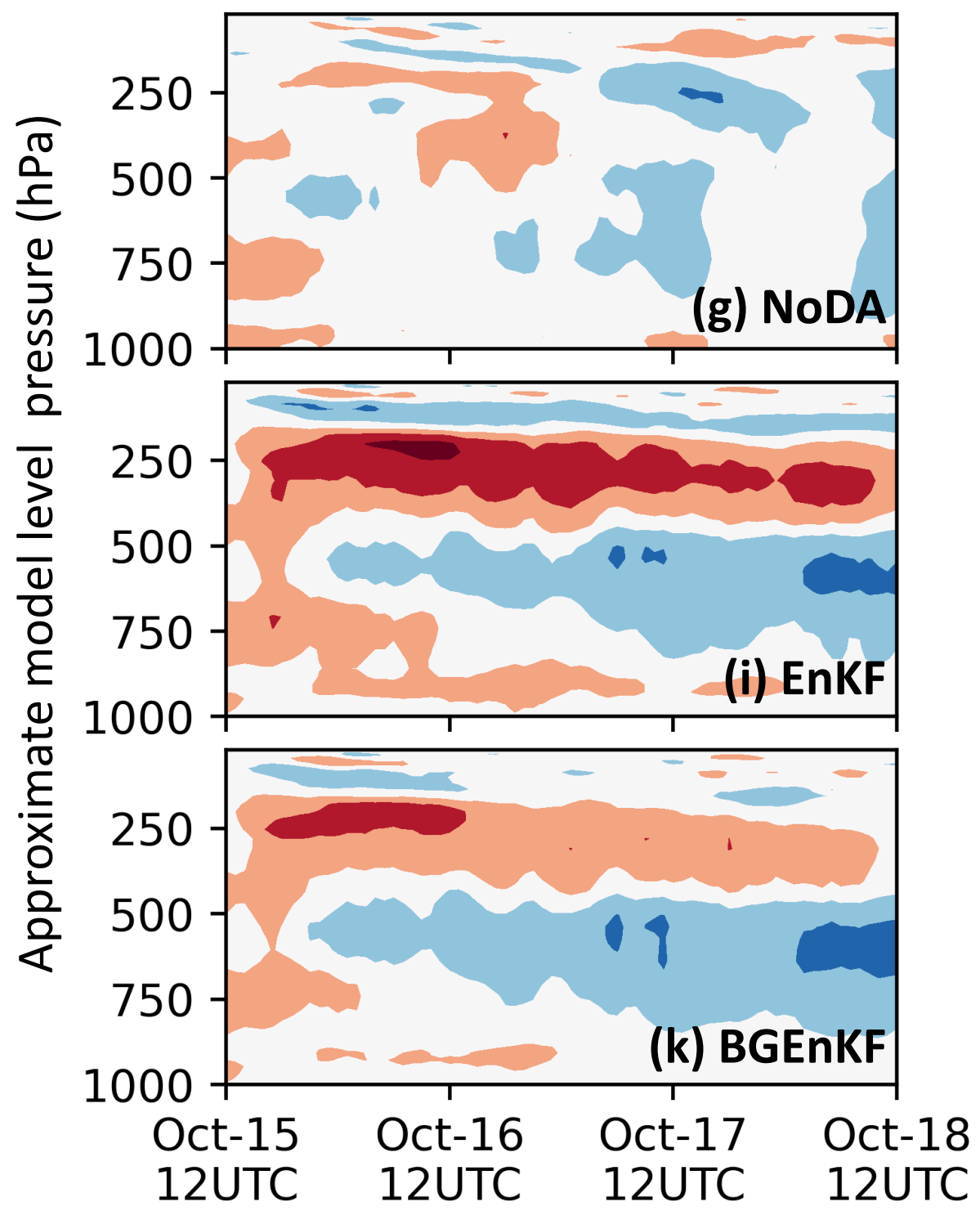
Zonal wind norm. biases



Meridional wind norm. biases



Temperature norm. biases



QVAPOR norm. biases

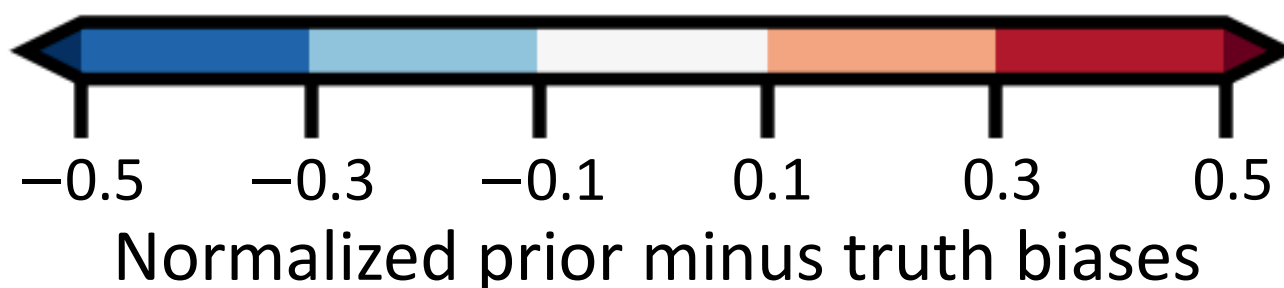
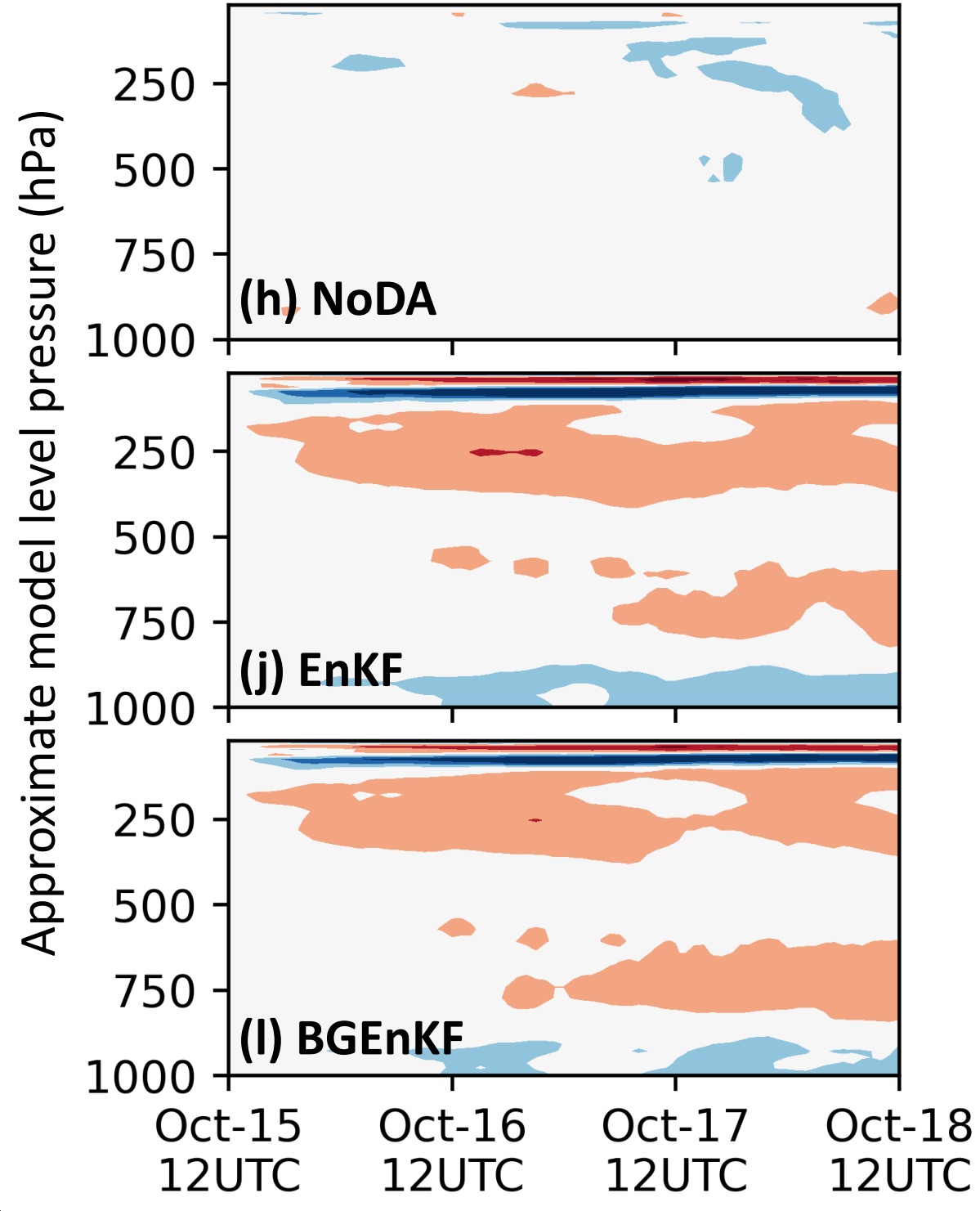
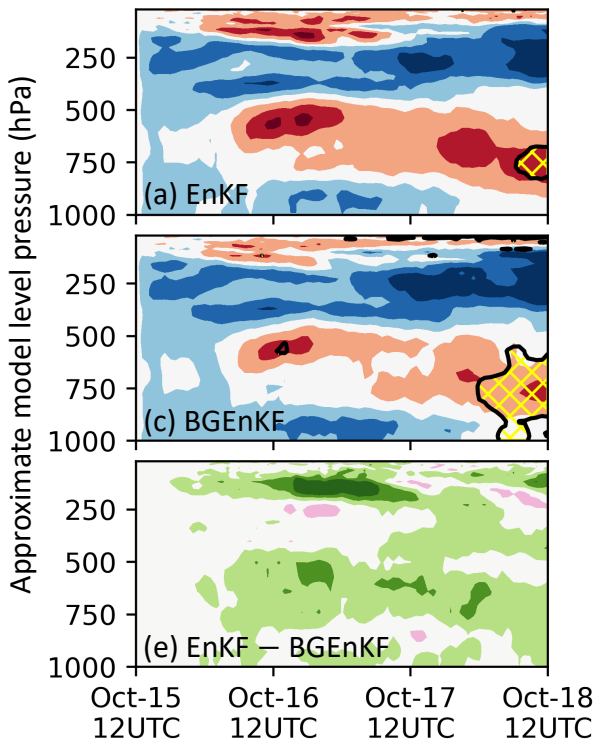
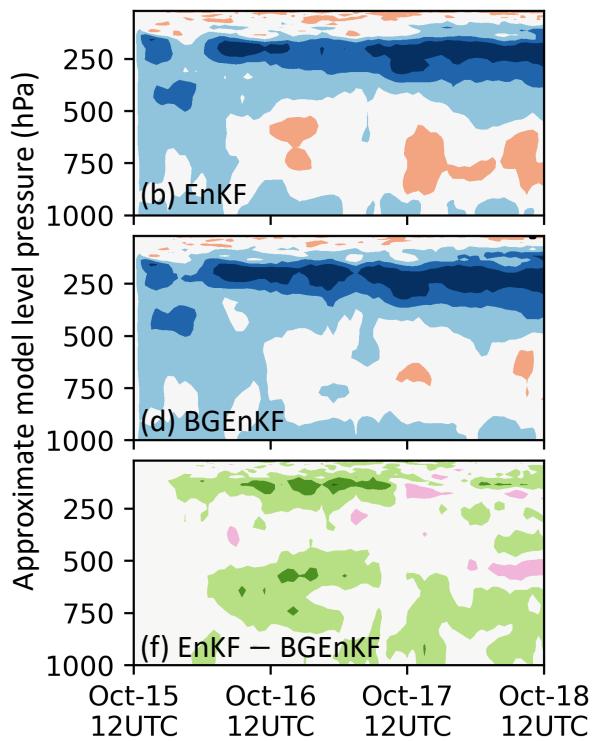


Figure 3.

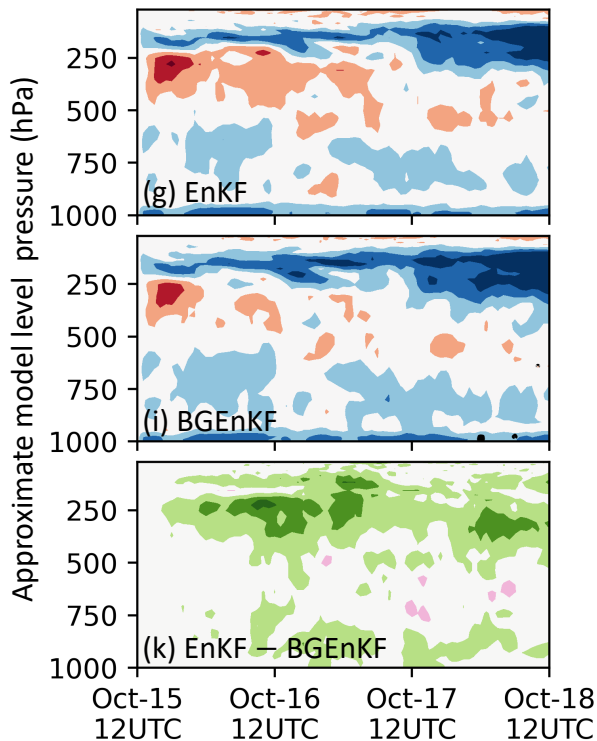
Zonal wind nRMSEs



Meridional wind nRMSEs



Temperature nRMSEs



QVAPOR nRMSEs

